

# Is There Any Improvement in Simulation of the Wintertime Western Pacific Teleconnection Pattern and Associated Climate Anomalies in CMIP6 Compared to CMIP5 Models?

HASI ARU,<sup>a,b</sup> WEN CHEN,<sup>a,b</sup> AND SHANGFENG CHEN<sup>a,b</sup>

<sup>a</sup> Center for Monsoon System Research, Institute of Atmospheric Physics, Chinese Academy of Sciences, Beijing, China

<sup>b</sup> College of Earth and Planetary Sciences, University of Chinese Academy of Sciences, Beijing, China

(Manuscript received 7 January 2021, in final form 26 July 2021)

**ABSTRACT:** The western Pacific pattern (WP) is one of the most important atmospheric teleconnections over the Northern Hemisphere (NH) in boreal winter and plays key roles in regulating weather and climate variations over many parts of the NH. This study evaluates the ability of the coupled models participating in CMIP5 and CMIP6 to capture the spatial pattern, dominant frequency, and associated climate anomalies of the winter WP. Ensemble means of the CMIP5 and CMIP6 models well capture spatial structures of the WP, with slightly higher skills for the CMIP6. However, the northern (southern) center of the WP is shifted westward (eastward) relative to the observations, and the strength of the northern center is overestimated in most CMIP5 and CMIP6 models. CMIP6 shows an improvement in simulating the dominant periodicity of the WP. WP-related climatic anomalies in most parts of the NH can be well simulated. However, there exists a large spread across the models in simulating surface air temperature (SAT) anomalies in the Russian Far East and northwest North America, which is attributable to the diversity of the intensity of the WP's northern lobe. Most CMIP5 and CMIP6 models largely overestimate the WP-related precipitation anomalies over Siberia, which is partly due to the overestimation of mean precipitation there. Furthermore, most models simulate a close relation of the WP and Arctic Oscillation (AO), which does not exist in observation. The CMIP5 and CMIP6 models with weak WP–AO relations have better ability than the models with strong WP–AO relations in capturing the WP-related SAT and precipitation anomalies over the NH, especially over Eurasia.

**KEYWORDS:** Coupled models; Spectral analysis/models/distribution; Climate variability; Climate classification/regimes

## 1. Introduction

In recent decades, substantial studies have explored an intriguing phenomenon termed “atmospheric teleconnections,” which refers to a large-scale recurrent low-frequency atmospheric circulation with a striking similarity of spatial structure and spanning vast geographic areas (Panagiotopoulos et al. 2002; Nigam 2003; Nigam and Baxter 2015; Feldstein and Franzke 2017; Chen et al. 2020). Studies indicated that the occurrence and persistence of extreme weather and climate events over many regions of the Northern Hemisphere are suggested to be largely attributed to the atmospheric teleconnections (Ning and Bradley 2015; Piao et al. 2016; Yang et al. 2018; Zhao et al. 2019). Therefore, a better understanding of the atmospheric teleconnection patterns is of great importance to improve the seasonal predictions of the weather and climate anomalies.

Wallace and Gutzler (1981) were the first to provide a comprehensive description of the five major teleconnection patterns in the Northern Hemisphere, which include the western Pacific pattern (WP). The signatures of the WP are featured by a meridional atmospheric dipole anomaly pattern with a positive southern lobe and a negative northern lobe of stronger amplitude

during its positive phase (Linkin and Nigam 2008; Nishii et al. 2010; Tanaka et al. 2016). On one hand, studies indicated that the WP is an internal dynamical mode with a barotropic vertical structure (Blackmon et al. 1979; Hsu and Wallace 1985; Nakamura et al. 1987). Barotropic process due to synoptic-scale transient eddies feedback and baroclinic energy conversion process both play important roles in the development and maintenance of the WP (Blackmon et al. 1979; Hsu and Wallace 1985; Nakamura et al. 1987; Lau 1988; Lau and Nath 1991; Rivière 2010; Tanaka et al. 2016; Sung et al. 2020). On the other hand, external forcings, such as sea surface temperature (SST) and Arctic sea ice anomalies, also partly contribute to the variation of the WP. For instance, Horel and Wallace (1981) indicated that SST anomalies in the tropical Pacific related to El Niño–Southern Oscillation (ENSO) contribute partly to the formation of the WP via heating-induced atmospheric Rossby wave train. Interest in this intriguing WP–ENSO relationship has been sparked by the observation that frequent occurrence of central Pacific ENSO is closely associated with the North Pacific climate variability (Yu and Kim 2011; Yeh et al. 2015, 2018; Park et al. 2018; Wang et al. 2019). Observational studies also suggest that the central Pacific ENSO-related SST anomalies are conducive to the formation of the WP-like pattern (Di Lorenzo et al. 2010; Furtado et al. 2012). Moreover, Nakamura et al. (2015) suggested that Arctic sea ice anomalies generated by preceding winter North Atlantic Oscillation could induce a WP-like atmospheric anomaly pattern in the following winter.

Fluctuation of the WP could exert notable impacts on weather and climate anomalies over Eurasia and North America. For instance, studies suggest that WP exerts a notable impact on the

Supplemental information related to this paper is available at the Journals Online website: <https://doi.org/10.1175/JCLI-D-21-0016.s1>.

Corresponding author: Shangfeng Chen, [chenshangfeng@mail.iap.ac.cn](mailto:chenshangfeng@mail.iap.ac.cn)

SAT anomalies over the Russian Far East and North America (NA) (Takaya and Nakamura 2005a,b; Linkin and Nigam 2008; Lim and Kim 2013). Aru et al. (2021) reported a robust impact of wintertime WP on the SAT anomalies over Eurasia and North America according to different definitions of the WP indices. In addition to the mean climate, variation of WP also contributes to the occurrence of extreme climate events. For example, Baxter and Nigam (2015) and Yu and Zhang (2015) consistently found that the occurrence of the record-breaking extreme 2013/14 cold winter in east-central North America is attributed largely to the extreme strength and prolonged duration of the WP event. Studies indicated that WP impacts extreme precipitation events over the Pacific and North American regions via modulating the meridional displacement of the subtropical jet stream and storm track activity over North Pacific (Nigam 2003; Linkin and Nigam 2008; Wettstein and Wallace 2010; Li and Wettstein 2012; Yuan et al. 2015). Moreover, interdecadal changes in the spatial structure of the WP have a pronounced impact on the extremely warm and cold temperature events in North America (Sung et al. 2019).

As an essential constituent of the Northern Hemisphere climate system, the WP was relatively less studied compared with the other major teleconnection patterns over Northern Hemisphere, such as the Arctic Oscillation (AO), North Atlantic Oscillation, and Pacific–North America teleconnection patterns (cf. Wallace 2000; Yu et al. 2007; Johnson et al. 2008; Lee et al. 2012; Moore et al. 2013; Lim and Kim 2016; Xu et al. 2016; Chen et al. 2017; Dai et al. 2017; Chen et al. 2019; Li et al. 2019). Given the marked impact of WP, realistically characterizing the spatiotemporal features of the WP, as well as the associated climate anomalies over the Northern Hemisphere in the state-of-the-art climate models, are essential for exploring regional climate variability, change and predictability, and evaluating the performance of climate models. Based on a suite of Coupled Model Intercomparison Project phase 5 (CMIP5) and phase 6 (CMIP6) historical model simulations, this study will address the following questions: 1) How well do the coupled models in CMIP5 and CMIP6 simulate the spatial patterns (including horizontal and vertical structures) of the WP in boreal winter? 2) Can CMIP5 and CMIP6 models reproduce the observed dominant periodicity of the WP? 3) Do CMIP6 models show improvements in the representations of the WP in terms of the spatial structures and temporal variations compared to the CMIP5 models? 4) Can SAT and precipitation anomalies related to the WP over Eurasia and North America be simulated by the CMIP5 and CMIP6 models?

In this framework, we introduce the data and methods in section 2. Section 3 assesses and compares the performances of the models in CMIP5 and CMIP6 in simulating the spatiotemporal features of WP. The ability of the models in capturing the WP-related SAT and precipitation anomalies over Eurasia and North Atlantic are examined in section 4. In section 4, we also examine the connections between WP and AO and investigate the impact of the WP–AO relation on the performance of the models in simulating the WP-related climatic anomalies. A summary and discussion are presented in section 5.

## 2. Data and methodology

### a. Observational data

Our baseline dataset is the National Centers for Environmental Prediction (NCEP)–National Center for Atmospheric Research (NCAR) reanalysis dataset with a horizontal resolution of  $2.5^\circ \times 2.5^\circ$  and extends from 1000 to 10 hPa with 17 pressure levels, available from 1948 onward (Kalnay et al. 1996). The present study also uses the monthly mean SAT and precipitation data from the University of Delaware, which are available from January 1900 to December 2017 and have a horizontal resolution of  $0.5^\circ \times 0.5^\circ$  (Willmott and Matsuura 2001). For the convenience of description, the variables from the NCEP–NCAR reanalysis and SAT and precipitation from the University of Delaware are considered as “observational” data in this study.

### b. Model outputs

This study employs the outputs from 27 CMIP5 and 26 CMIP6 historical simulations. Brief descriptions of the CMIP5 (Taylor et al. 2012) and CMIP6 (Eyring et al. 2016) models including their modeling centers and horizontal resolutions are listed in Table 1 and Table 2, respectively. Following previous studies (e.g., Kucharski and Joshi 2017; Joshi and Ha 2019), only the first realization (i.e., the r1i1p1 integration for CMIP5, and r1i1p1f1 for CMIP6) for each model is analyzed for a fair comparison. To compare the model results with observations, all the variables have been interpolated to a common horizontal resolution of  $2.5^\circ \times 2.5^\circ$ . All of the observational and simulation data are first linearly detrended to remove the global warming signals. Then, anomalies are calculated by removing the long-term monthly climatology over the entire period analyzed here. The 3-month averages are calculated for the examination of the winter season [i.e., December–February (DJF)] during which the WP is most prominent.

### c. Statistical significance test

The regressions are calculated for each model respectively, and then the multimodel ensemble mean (MME) is obtained by averaging the regressed patterns. The standard two-tailed Student's *t* test is used to evaluate the significance levels of regression and correlation coefficients in observation and the individual model results. A bootstrap resampling method is adopted to evaluate the robustness of the differences between CMIP5 and CMIP6 model groups by constructing 10 000 random realizations of the multimodel mean (Austin and Tu 2004). In this process, one model is allowed to be selected again. For the individual model results, we also employed the bootstrap method as a nonparametric device to estimate the uncertainty by giving a specific confidence interval; here we utilized a 95% confidence level. Considering the limited number of observations and model members, for a given predictor variable, we inspect the distribution of the associated regression coefficients across the 1000 bootstrap samples. In addition, according to the previous studies (Deser et al. 2012; Kucharski and Joshi 2017; Joshi and Ha 2019; Chen et al. 2021; Zheng et al. 2021), we evaluate the 95% statistical significance of the ensemble mean anomalies obtained from regression

TABLE 1. List of the 27 CMIP5 models, with respective institution and model horizontal resolution. (Expansions of most acronyms are available online at <http://www.ametsoc.org/PubsAcronymList>.)

Model ID	Model acronym	Institution	Resolution (lon × lat)
1	BCC-CSM1.1	Beijing Climate Center, China Meteorological Administration, China	2.8° × 2.8°
2	BCC-CSM1.1.M	Beijing Climate Center, China Meteorological Administration, China	2.8° × 2.8°
3	BNU-ESM	GCESS, BNU, China	2.8° × 2.8°
4	CCSM4	National Center for Atmospheric Research, Boulder, United States	1.25° × 0.9°
5	CESM1(BGC)	National Science Foundation (NSF)–U.S. Department of Energy (DOE)–NCAR, United States	1.25° × 0.9°
6	CESM1(CAM5)	NSF/DOE National Center for Atmospheric Research, Boulder, United States	1.25° × 0.9°
7	CMCC-CM	Centro Euro-Mediterraneo per I Cambiamenti Climatici (CMCC), Italy	0.75° × 0.75°
8	CSIRO-Mk3.6.0	CSIRO–Queensland Climate Change Centre of Excellence (QCCCE), Australia	1.875° × 1.875°
9	FGOALS-g2	Institute of Atmospheric Physics, Chinese Academy of Sciences, Tsinghua University, China	2.8° × 2.8°
10	FIO-ESM	The First Institution of Oceanography, China	2.8° × 2.8°
11	GFDL-CM3	National Oceanic and Atmospheric Administration (NOAA)/Geophysical Fluid Dynamics Laboratory (GFDL), United States	1.25° × 2°
12	GFDL-ESM2G	NOAA/GFDL, United States	1.25° × 2°
13	GFDL-ESM2M	NOAA/GFDL, United States	1.25° × 2°
14	GISS-E2-H	National Aeronautics and Space Administration (NASA) Goddard Institute for Space Studies (GISS), United States	1.25° × 2°
15	GISS-E2-R	NASA GISS, United States	1.25° × 2°
16	HadGEM2-AO	National Institute of Meteorological Research (NIMR), Korea Meteorological Administration (KMA), South Korea	1.875° × 1.25°
17	HadGEM2-CC	UKMO Hadley Centre, United Kingdom	1.875° × 1.25°
18	HadGEM2-ES	UKMO Hadley Centre, United Kingdom	1.875° × 1.25°
19	IPSL-CM5A-LR	L'Institut Pierre-Simon Laplace (IPSL), France	1.9° × 3.8°
20	MIROC-ESM	AORI-NIES-JAMSTEC, Japan	2.8° × 2.8°
21	MIROC-ESM-CHEM	AORI-NIES-JAMSTEC, Japan	2.8° × 2.8°
22	MIROC5	Atmosphere and Ocean Research Institute (AORI)–National Institute for Environmental Studies (NIES)–Japan Agency for Marine–Earth Science and Technology (JAMSTEC), Japan	1.4° × 1.4°
23	MPI-ESM-LR	Max Planck Institute for Meteorology (MPI-M), Germany	1.875° × 1.875°
24	MPI-ESM-MR	MPI-M, Germany	1.875° × 1.875°
25	MRI-CGCM3	Meteorological Research Institute (MRI), Japan	1.125° × 1.125°
26	NorESM1-M	Norwegian Climate Centre (NCC), Norway	2.5° × 1.875°
27	NorESM1-ME	NCC, Norway	2.5° × 1.875°

analyses against a null hypothesis of zero change when they meet the following criterion, which is based on the one-sample  $t$  test:

$$t(N-1) = \frac{\bar{X}}{\sigma/\sqrt{N}}, \quad (1)$$

where  $\bar{X}$  and  $\sigma$  denote the ensemble mean and standard deviation of the anomalies of variables among multimodel, respectively. The corresponding  $t(N-1)$  is the degree of freedom  $N-1$  of  $t$  statistic, in which  $N$  stands for the ensemble size [27 (26) for CMIP5 (CMIP6) in this study]. Then, when  $\bar{X}$  and  $\sigma$  satisfy the following criterion

$$|\bar{X}| \geq \frac{\sigma \times t(N-1)_{p=0.05}}{\sqrt{N}} \quad (2)$$

the ensemble mean changes are significant at the 95% confidence level. With the ensemble size of  $N = 27$  (26), the value of  $t(N-1)_{p=0.05}$  can be approximately taken as 2 for a two-sided

$t$  test. Thus, in this context, we assign the  $t$  value to a constant  $\lambda$  that is equal to 2.

#### d. Index definitions

The representation of the WP index is calculated in the following steps. An EOF analysis is performed on the observed and linearly detrended winter 500-hPa geopotential height (Z500) over the western North Pacific region (20°–70°N, 120°–180°E) during 1949/50–2004/05. Then the first EOF mode stands for the WP pattern as generally defined in previous studies (Nishii et al. 2010). Finally, the observed WP index is obtained by projecting the observed and detrended winter Z500 anomalies onto the aforementioned EOF mode. Meanwhile, the WP indices in CMIP5 and CMIP6 model simulations are obtained by projecting the model detrended wintertime Z500 anomalies onto the observed EOF spatial pattern. That is, we used the common basis function (CBF) to evaluate the performance of the models in simulating the WP, which applicability for model simulation as has been demonstrated in many previous studies (Bonfils et al. 2015;

TABLE 2. List of the 26 CMIP6 models, with respective institution and model horizontal resolution.

Model ID	Model acronym	Institution	Resolution (lon $\times$ lat)
1	ACCESS-CM2	CSIRO-ARCCSS (Australian Research Council Centre of Excellence for Climate System Science)	$1.25^\circ \times 1.875^\circ$
2	ACCESS-ESM1-5	Commonwealth Scientific and Industrial Research Organization, Australia	$1.25^\circ \times 1.875^\circ$
3	BCC-CSM2-MR	Beijing Climate Center, China Meteorological Administration, China	$1.125^\circ \times 1.125^\circ$
4	BCC-ESM1	Beijing Climate Center, China Meteorological Administration, China	$2.8^\circ \times 2.8^\circ$
5	CAMS-CSM1-0	Chinese Academy of Meteorological Sciences, Beijing, China	$1.125^\circ \times 1.125^\circ$
6	CESM2	National Center for Atmospheric Research, Climate and Global Dynamics Laboratory, United States	$0.9^\circ \times 1.25^\circ$
7	CESM2-WACCM	National Center for Atmospheric Research, Climate and Global Dynamics Laboratory, United States	$0.9^\circ \times 1.25^\circ$
8	CMCC-CM2-SR5	Fondazione Centro Euro-Mediterraneo sui Cambiamenti Climatici, Italy	$0.9^\circ \times 1.25^\circ$
9	CIESM	Department of Earth System Science, Tsinghua University, Beijing, China	$0.9^\circ \times 1.25^\circ$
10	E3SM-1-0	E3SM Project	$1.0^\circ \times 1.0^\circ$
11	E3SM-1-1	E3SM Project	$1.0^\circ \times 1.0^\circ$
12	E3SM-1-1-ECA	E3SM Project	$1.0^\circ \times 1.0^\circ$
13	EC-Earth3	EC-Earth Consortium	$0.7^\circ \times 0.7^\circ$
14	FGOALS-g3	Chinese Academy of Sciences, Beijing, China	$2.25^\circ \times 2^\circ$
15	FIO-ESM-2-0	FIO (First Institute of Oceanography, State Oceanic Administration, China), QNLM (Qingdao National Laboratory for Marine Science and Technology, China)	$0.9^\circ \times 1.25^\circ$
16	GFDL-ESM4	National Oceanic and Atmospheric Administration, Geophysical Fluid Dynamics Laboratory, United States	$1.0^\circ \times 1.25^\circ$
17	GISS-E2-1-G	Goddard Institute for Space Studies, New York, United States	$2.0^\circ \times 2.5^\circ$
18	INM-CM5-0	Institute for Numerical Mathematics, Russian Academy of Science, Russia	$1.5^\circ \times 2.0^\circ$
19	IPSL-CM6A-LR	Institute Pierre Simon Laplace, France	$1.25^\circ \times 2.5^\circ$
20	MIROC6	AORI-NIES-JAMSTEC, Japan	$1.4^\circ \times 1.4^\circ$
21	MPI-ESM1-2-HR	Max Planck Institute for Meteorology (MPI-M), Germany	$0.9^\circ \times 0.9^\circ$
22	MPI-ESM1-2-LR	Max Planck Institute for Meteorology (MPI-M), Germany	$1.875^\circ \times 1.875^\circ$
23	MRI-ESM2-0	Meteorological Research Institute, Tsukuba, Japan	$1.125^\circ \times 1.125^\circ$
24	NESM3	Nanjing University of Information Science and Technology (NUIST), Nanjing, China	$1.875^\circ \times 1.875^\circ$
25	NorESM2-LM	Norwegian Climate Centre (NCC), Norway	$1.875^\circ \times 2.5^\circ$
26	SAM0-UNICON	Seoul National University, Seoul, South Korea	$0.9^\circ \times 1.25^\circ$

Wang et al. 2015; Lee et al. 2019). The CBF approach circumvents the issues of conventional EOF analysis, for example, eliminating corrections of arbitrary sign differences for the EOFs or PCs being compared (Lee et al. 2019). It also side-steps the problems that for some models, in which the first EOF is more similar to a higher-order model EOF, or even that the first EOF of the model does not capture the characteristics of the WP. Similar methods are used to define the AO index in the observation and coupled model simulations but apply to the detrended sea level pressure anomalies north of  $20^\circ\text{N}$  in the Northern Hemisphere. Furthermore, we also use a series of indices to describe WP's characteristics. For example, the intensity of each center of WP is computed as the nine-points-mean of central GPH anomalies (i.e., the maximum or minimum plus eight values of nearest grid points located on diagonal and orthogonal), the locality of the WP south lobe (WPsl) and WP north lobe (WPnl) are determined by the position of the maximum or minimum value of the positive WP regression spatial pattern, respectively.

The simulation performance of the climatology WP pattern over western North Pacific ( $20^\circ\text{--}80^\circ\text{N}$ ,  $120^\circ\text{E}\text{--}120^\circ\text{W}$ ) is evaluated

based on the following formula (Taylor 2001; Hirota et al. 2011; Chen et al. 2013):

$$S = \frac{(1 + R)^2}{(\sigma_f + 1/\sigma_f)^2},$$

where  $R$  denotes the pattern correlation coefficient between the observation and individual model, and  $\sigma_f$  denotes the ratio of spatial standard deviations of the models against that of the observation. Apparently, both the spatial distribution and magnitude have been considered in the expression while comparing model results with observations. Typically, for the ideal case, since  $R$  equals 1 and as the simulated standard deviation approaches the observed counterpart (i.e.,  $\sigma_f \rightarrow 1$ ) the skill score  $S$  approaches unity. With a given ratio of spatial standard deviation, the skill score increases monotonically with increasing correlation; for a given correlation, the skill score increases as the simulated standard deviation approach the observed one, which always ranges from 0 to 1. Furthermore, this skill score quantifies the overall correspondence between models



and observations, with lower skill scores in overestimated and underestimated models.

### 3. Spatiotemporal characteristics of the WP: Observations versus model simulations

This section first examines the capability of the CMIP5 and CMIP6 models in portraying the horizontal and vertical structures of the wintertime WP. Figure 1a displays the spatial distribution of the wintertime Z500 and 500-hPa wind anomalies obtained by regression upon the normalized WP index in the observation. The positive phase of the winter WP shows marked negative Z500 and outstretched cyclonic circulation anomalies extending from mid- to high-latitude Eurasia to the coast of western North America, along with pronounced positive Z500 and anticyclonic circulation anomalies over the western North Pacific (Fig. 1a). Statistical significance tests verify the features of the WP in observations in Fig. 1a, with the regression coefficients exceeding 95% confidence level based on the bootstrap test (not shown). Anomalies described below in this paper correspond to the positive phase of the WP unless otherwise stated. From the inspection of the spatial patterns and circulation associated with WP, the observed WP is well captured by the MMEs of the CMIP5 and CMIP6 models (Figs. 1b,c). Nevertheless, the MMEs overestimate the WP-related negative geopotential height and circulation anomalies in the Arctic and slightly underestimate the counterparts in southeastern North America (Figs. 1b,c). It is noted that the overestimated negative anomaly is reminiscent of the Arctic Oscillation (AO) (Thompson and Wallace 1998 2000). Thus, we presume that the spatial pattern biases of the WP might be affected by the relationship between WP and AO, which is discussed in further detail in section 5.

To quantitatively examine the performances of the CMIP5 and CMIP6 models in capturing the spatial structure of WP, the pattern correlation coefficients and normalized standard deviations of the winter Z500 anomalies over 20°–80°N, 120°E–120°W are shown in a Taylor diagram (Fig. 2a). Note that the standardized deviation is defined as the ratio of the standard deviation obtained from individual models to the standard deviation derived from the observation. The pattern correlation coefficients range from 0.78 to 0.98 among individual models (Fig. 2a), indicating the reasonable simulations of the observational WP among models. The intermodel spreads of the normalized standard deviation are reduced from CMIP5 (0.71–1.56) to CMIP6 (0.84–1.52). Additionally, the MME manifests a better capability than most of the individual models in reproducing the pattern correlation [the CMIP5 (CMIP6) MME pattern correlation is 0.97 (0.96)] and the normalized standard deviation [the CMIP5 (CMIP6) MME standard deviation is 0.99 (1.06)] of the winter WP (Fig. 2a).

Does CMIP6 show an improvement over CMIP5 in capturing the spatial patterns of the winter WP? Figure 2b shows the box-and-whisker plot of the skill scores of CMIP5 and CMIP6 models for the WP spatial pattern. It shows that the CMIP6 models exhibit less dispersion of skill scores than the CMIP5 models. The skill score ranges from 0.75 to 0.97 in the CMIP5 models, while it ranges from 0.78 to 0.97 in the

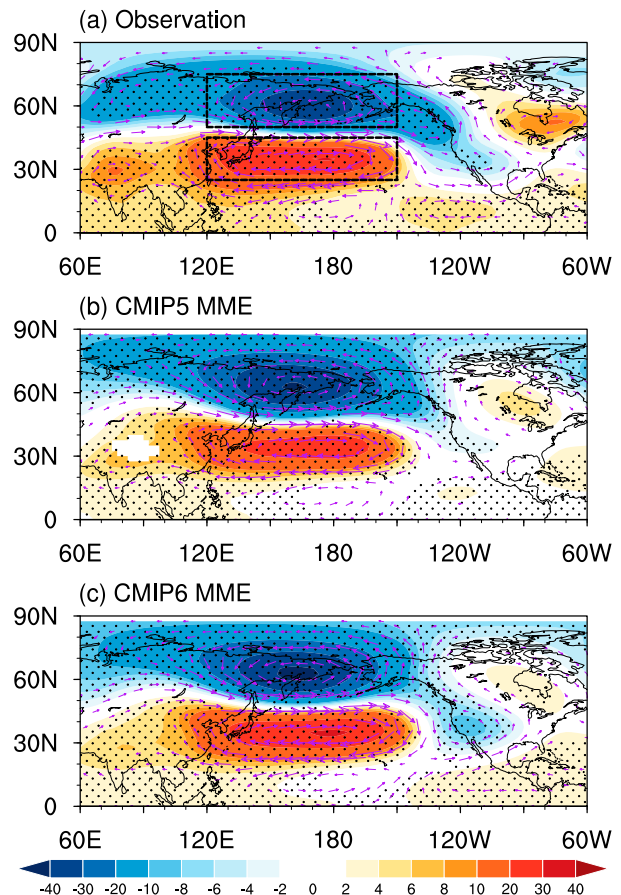


FIG. 1. Anomalies of 500-hPa geopotential height (Z500; units: m) and the corresponding circulations (UV500, units:  $\text{m s}^{-1}$ ) obtained through regressing upon the WPI during 1950–2005 for the (a) observation, (b) MME of CMIP5, and (c) MME of CMIP6 historical simulations. The anomalies that are significantly different from zero at the 95% confidence level are stippled.

CMIP6 models. In addition, for the median and multimodel mean (hereinafter referred to as the MMM), the skill scores of the WP in CMIP6 (0.90 and 0.887) are slightly higher than those for the CMIP5 counterpart (0.88 and 0.881). This slight increase in skill score for CMIP6 is tested to be significant according to the bootstrap test. Thus, the above evidence indicates an improvement in the ability of the latest climate models to simulate the horizontal structure of the winter WP.

Performances of the models in reproducing the vertical structure of the WP are further examined. Studies have demonstrated that the circulation anomalies associated with the WP display an equivalent barotropic vertical structure throughout the troposphere (e.g., Hsu and Wallace 1985; Tanaka et al. 2016). Figure 3 displays latitude–height cross section of the geopotential height anomalies averaged over 120°E–150°W obtained by regression upon the normalized WP index for the observation, MMEs of CMIP5 and CMIP6 models. There displays a quasi-barotropic vertical dipole structure with strong negative geopotential height anomalies around 60°N and positive geopotential height anomalies

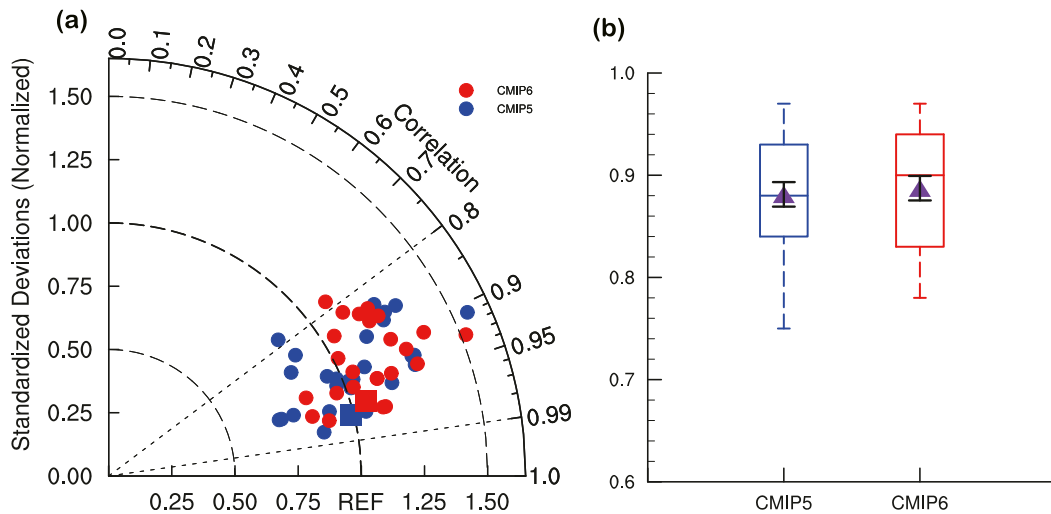


FIG. 2. (a) Taylor diagram of CMIP5 (blue dots) and CMIP6 (red dots) winter Z500 anomalies over the North Pacific ( $20^{\circ}$ – $80^{\circ}$ N,  $120^{\circ}$ E– $120^{\circ}$ W) as shown in Fig. 1. The blue and red squares stand for the MME of CMIP5 and CMIP6, respectively. The pattern correlation between the observation WP and WP in CMIP5 and CMIP6 models is represented by the azimuthal position. The radius distance denotes the ratio of the standard deviation obtained from CMIP5 and CMIP6 modes to the standard deviation from observation. (b) Box-and-whisker plots depicting the distribution of CMIP5 (blue box) and CMIP6 (red box) models' skill scores in reproducing the climatology of the WP pattern. The skill score of WP pattern is calculated based on the equation proposed by Chen et al. (2013), which is mentioned in section 2c, over the region of  $20^{\circ}$ – $80^{\circ}$ N,  $120^{\circ}$ E– $120^{\circ}$ W. The solid purple triangle stands for the multimodel mean of the CMIP5 and CMIP6 historical simulation skill scores. The multimodel mean increment of skill score is 0.008, which is statistically significant above the 95% confidence level according to a bootstrap test. The error bars on the multimodel mean represents the 95% confidence level determined by a bootstrap test.

around  $30^{\circ}$ N through the troposphere for both CMIP5 and CMIP6 MMEs (Figs. 3b,c). Meanwhile, the amplitude of the WP in the CMIP6 MME (Fig. 3c) is more in line with the amplitude of the observations (Fig. 3a) compared to the CMIP5 MME (Fig. 3b).

To detect the amplitude of the WP, we calculate the WPnl and WPsl amplitude indices for the subpolar North Pacific ( $50^{\circ}$ – $75^{\circ}$ N,  $120^{\circ}$ E– $150^{\circ}$ W) and the subtropical North Pacific ( $25^{\circ}$ – $45^{\circ}$ N,  $120^{\circ}$ E– $150^{\circ}$ W) regions, representing the strength of the northern and southern lobes of the WP, respectively. In the observation, the northern lobe of the WP is stronger than that of the southern lobe. Both the CMIP5 and CMIP6 MMEs represent well the stronger northern lobe over the North Pacific, which is consistent with the observation (Fig. 4). As for the simulation of WPnl amplitude, both CMIP5 and CMIP6 MMEs overestimate the strength of WPnl. Particularly, WPnl amplitudes in 19 of the 27 CMIP5 and 22 of the 26 CMIP6 models are stronger than that in the observation. In addition, the observed WPnl amplitude lies within the box and slightly above the lower quartile in CMIP5 models, while for CMIP6 models it falls outside the box and lies beneath the lower quartile (Fig. 4 subplot). Hence, the above evidence indicates that CMIP5 and CMIP6 models tend to overestimate the strength of the WPnl. However, there is no consensus on the simulated strength of the WPsl in both sets of models, with an underestimation (overestimation) in the CMIP5 (CMIP6) models. Likewise, the simulated increments for WP north and south lobe amplitudes are 1.3 and 5.0 m, respectively, both greater than the 97.5%

interquartile of 1.06 and 3.81 m, indicating statistical significance above the 95% confidence level.

In the following, we further examine the performance of the models in capturing locations of the WP's northern and southern centers. Figure 5 gives a sketch of the locations of the WP for the individual CMIP5 and CMIP6 models, as well as their MMEs. In the observations, the center of the maximum (minimum) Z500 anomalies over the subtropical (subpolar) North Pacific [i.e., the south (north) lobe] is located near  $35^{\circ}$ N,  $175^{\circ}$ E ( $60^{\circ}$ N,  $167.5^{\circ}$ E). It is noteworthy that the center of the MME south lobe appears  $2.5^{\circ}$  of longitude to the east (Fig. 5b). Conversely, in the MME, the north lobe appears  $2.5^{\circ}$  latitude to the north and  $5^{\circ}$  longitude to the west (Fig. 5a). CMIP6 models show an improvement in reproducing the location of the WP with relatively smaller uncertainty in the zonal position. It should be mentioned that although the MME WP patterns are closely similar to the observations, there is large intermodel diversity in terms of the zonal and meridional position. The factors contributing to this diversity will be discussed later.

Next, we assess the temporal characteristics of the WP in the model simulations by applying spectral analysis to the normalized WP indices. The observations display significant power spectra on interannual time scales, with four dominant peaks in the 2–4-, 4–6-, and 6–8-yr ranges, respectively (Fig. 6c). In the range of the interannual variability, all the individual models in CMIP5 can simulate significant changes in the power spectrum, with 7 out of 27 models having stronger power than the observed power spectrum (Fig. 6a).

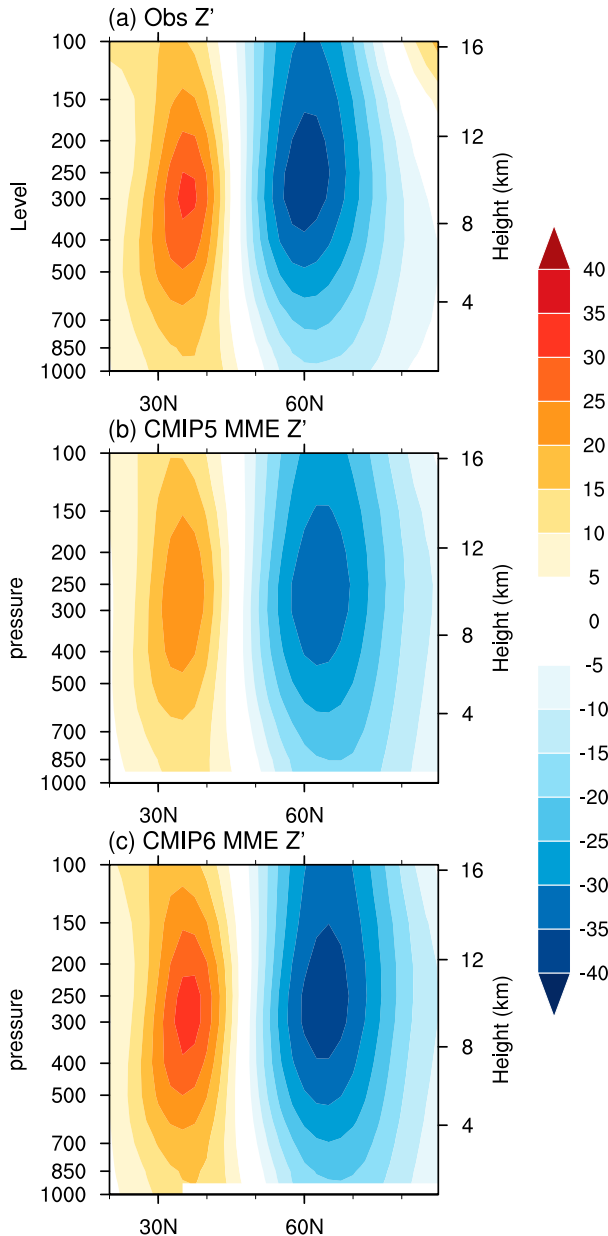


FIG. 3. Latitude–height profiles of the wintertime geopotential height anomalies (units: m) over 120°E–150°W obtained by regression upon the normalized WP index in (a) observations, (b) MME of the 27 CMIP5 models, and (c) MME of the 26 CMIP6 models.

From CMIP5 to CMIP6, there has been an overall reduction in the intermodel variability of the period, with much of the power limited to the 2–10-yr range (Fig. 6b). Figure 6c depicts the power spectrum of the MMEs for CMIP5 and CMIP6. It is clear that the CMIP6 MME spectrum resembles the observation more closely, with power peaks occurring around 4–6 and 12 years; conversely, the spectral peak of the CMIP5 MME shifts to the 8–12-yr range, which relatively mismatches with the observations. This indicates that the CMIP6 models have

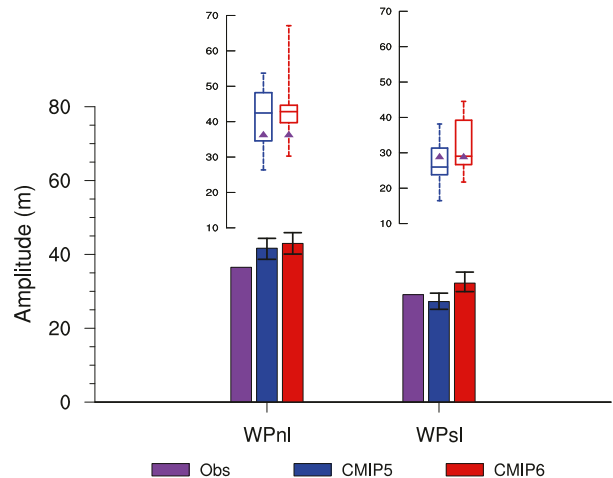


FIG. 4. Changes in the intensities of the WP south (WPsl, the maximum positive) and north lobes (WPnl, the maximum negative; the absolute values are shown here) based on the 500-hPa geopotential height anomalies (units: m) over the North Pacific as shown in Fig. 1. The purple bars denote the amplitude of the observations, the blue bars denote the amplitude of CMIP5 MME of historical simulations, and the red bars denote the amplitude of CMIP6 MME of historical simulations. The multimodel mean increment of 1.3 m for WPnl and 5.0 m for WPsl from CMIP5 to CMIP6 are both statistically significant above the 95% confidence level according to a bootstrap test. Error bars in the multimodel mean represents the 95% confidence level determined by a bootstrap test for CMIP5 and CMIP6, respectively. The subplot is the box-and-whisker plot for the CMIP5 and CMIP6 models simulated WPnl and WPsl amplitude. The solid purple triangle corresponds to the observed WP lobe's amplitude. The blue (red) boxes stand for the CMIP5 (CMIP6) model simulations.

an improved representation of the dominant periodicity of the WP compared to CMIP5. Additionally, both sets of models overestimate the interdecadal variability of WP.

#### 4. Climatic impacts of the WP simulated by the CMIP5 and CMIP6 models

In this section, we examine the capability of models to simulate the SAT and precipitation anomalies over the middle and high latitudes of the Northern Hemisphere, especially in Eurasia and North America. Pioneering studies uncovered that WP closely ties to the SAT variations in East Asia and North America (Takaya and Nakamura 2013; Lim and Kim 2013; Linkin and Nigam 2008; Baxter and Nigam 2015; Yu and Zhang 2015; Cheung and Zhou 2016; Dai and Tan 2019; Sung et al. 2019). Several studies have also revealed that WP has a significant impact on land and ocean rainfall over North America and the North Pacific (Linkin and Nigam 2008; Yuan et al. 2015).

##### a. Intermodel differences in areal surface air temperature anomalies

We inspect the surface air temperature anomalies captured by the coupled models with respect to the WP index (Fig. 7). It

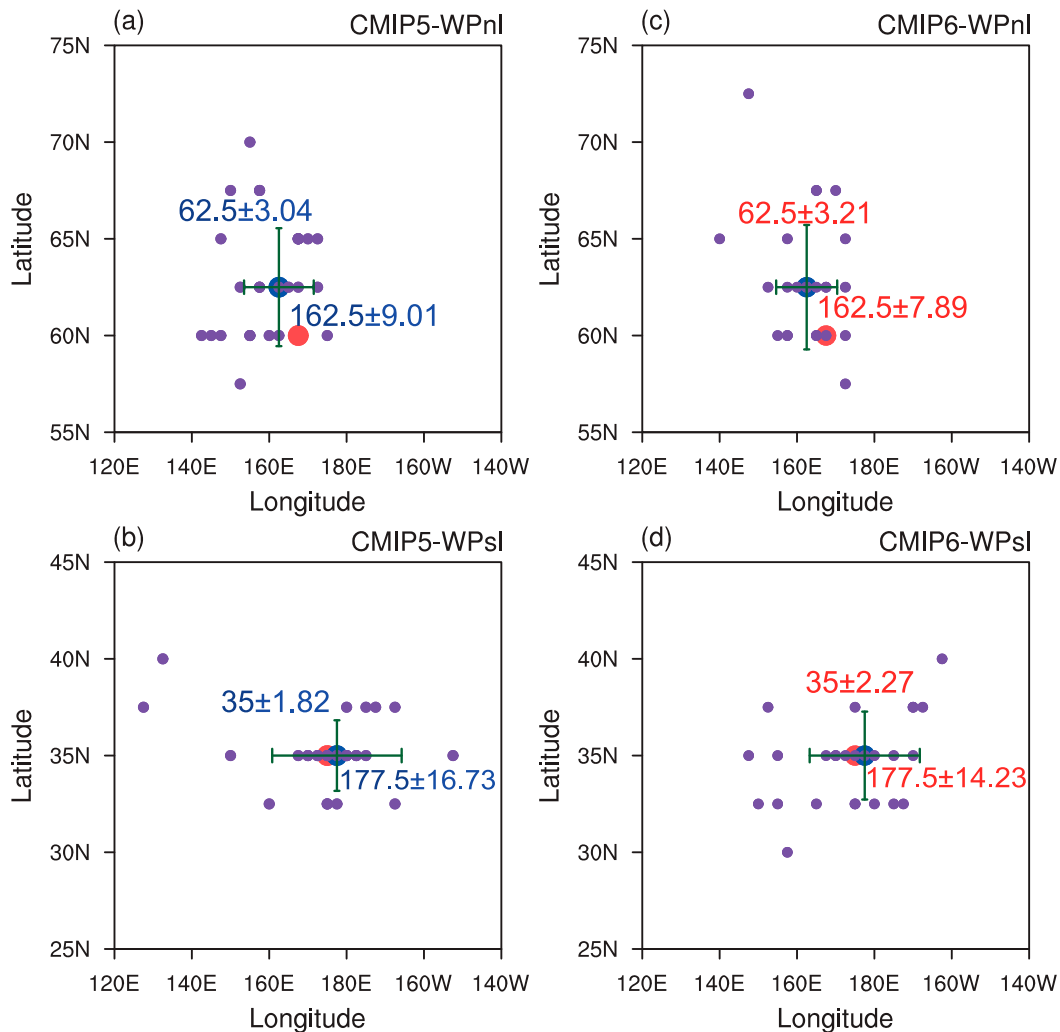


FIG. 5. Locations of the maximum value of 500-hPa geopotential height anomalies related to the (a) south lobe and (b) north lobe of WP in CMIP5 (purple dots) and observations (red dots). (c), (d) As in (a) and (b), but for the CMIP6 model outputs. The corresponding multimodel means and their one standard deviation of uncertainties are indicated by blue dots with error bars, with nearby values showing for the three variables mentioned in the abscissa and ordinate, respectively.

shows a generally similar distribution of winter WP-related SAT anomalies over Eurasia and North America, with negative SAT anomalies over the Russian Far East and southwestern United States, and positive SAT anomalies over midlatitude Southeast Asia and the Great Lakes. In contrast, the positive SAT anomalies over Southeast Asia extend northward toward the Lake Baikal region, and the amplitude of the MME is stronger in CMIP5 and CMIP6 MMEs compared to the observations (Figs. 7a,b,c). Additionally, the MME discerns the significant positive SAT anomalies over the Great Lakes but overestimates the anomalies extending northwestward into Alaska (Figs. 7b,c). Meanwhile, compared to the observed negative SAT anomalies over the Russian Far East, the negative SAT anomalies in the MMEs are much stronger (Figs. 7b,c).

To assess the ability of the coupled models to simulate the WP-related regional SAT anomalies, we calculate the model's

skill score in capturing SAT anomalies over Eurasia (EU; 20°–80°N, 60°E–180°) and North America (NA; 20°–80°N, 160°–60°W) according to the spatial correlations and the ratio of standard deviation between the model and observations, respectively. The skill score for each model and the CMIP5 and CMIP6 MMMs are represented by the box-and-whisker plots in Figs. 8a and 8b. In the EU region, the CMIP5 and CMIP6 models perform well in capturing the WP-related regional SAT anomalies, with the CMIP5 (CMIP6) model skill scores ranging from 0.02 to 0.88 (0.39 to 0.92). Irrespective of the outliers, CMIP6 corresponds to a slightly higher median and MMM (0.715 and 0.69) than CMIP5 (0.65 and 0.62) (Fig. 8a). It indicates an improved ability of CMIP6 to simulate SAT anomalies in the Eurasian region. For the NA regions, the CMIP6 models also show an improvement in the simulation of regional SAT anomalies (Fig. 8b), although the improvement



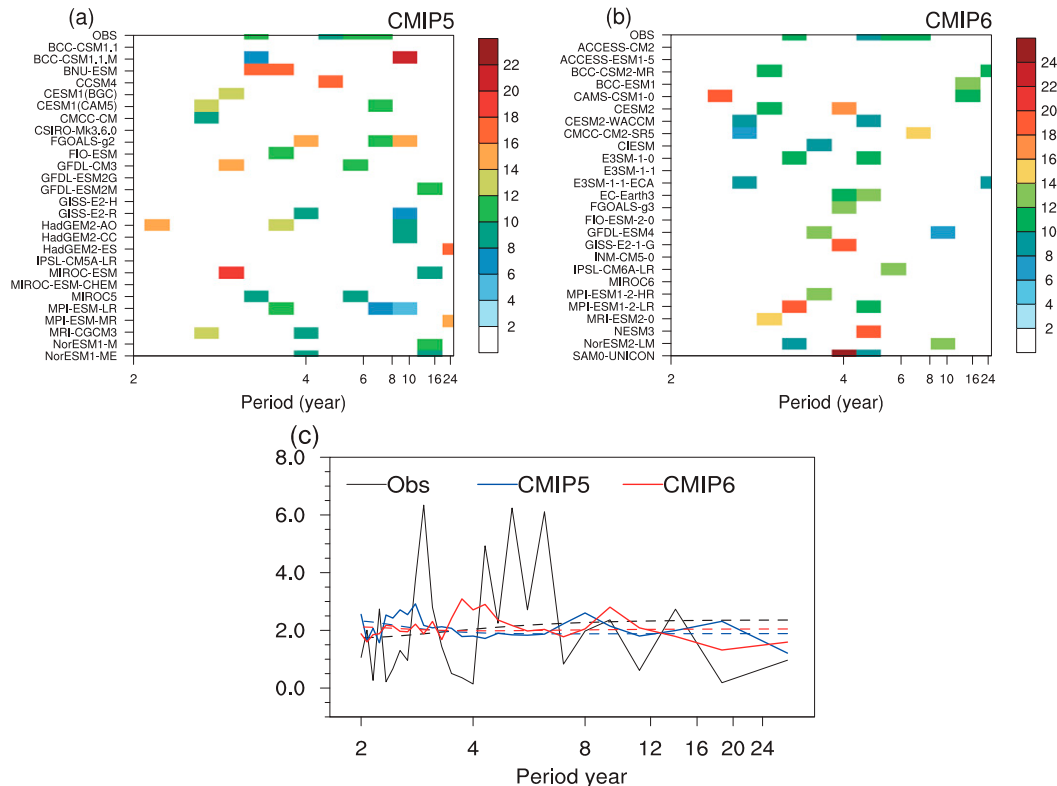


FIG. 6. (a) Power spectra (percentage of total variance explained) of the wintertime WP indices of CMIP5 historical simulations and observations during 1950–2005. Only significant power values (over the 90% confidence level) are shaded. (b) As in (a), but for the CMIP6 historical simulations. (c) Power spectrum distributions of the wintertime WP index of CMIP5 (blue solid curve) and CMIP6 (red solid curve) historical simulations and observations (black solid curve) during 1950–2005. The corresponding dashed line of the same colors represents the red noise confidence level.

is relatively less compared to that in the EU region (Fig. 8a). The incremental MMM of 0.08 (0.015) for the EU region (NA region) skill scores from CMIP5 to CMIP6 is greater than the 97.5% quantile of 0.03 (0.0095), indicating statistical significance above the 95% confidence level, which further justifies the significant improvement from CMIP5 to CMIP6.

For a quantitative comparison of the SAT anomalies related to the WP, we measure the areal SAT anomalies over five selected regions, including the Russian Far East region (RFE) ( $60^{\circ}$ – $70^{\circ}$ N,  $130^{\circ}$ – $160^{\circ}$ E), midlatitude southern Asia (MSA) ( $25^{\circ}$ – $45^{\circ}$ N,  $70^{\circ}$ – $115^{\circ}$ E), northwest North America (NNA) ( $55^{\circ}$ – $70^{\circ}$ N,  $165^{\circ}$ – $120^{\circ}$ W), the Great Lakes of North America (GLNA) ( $40^{\circ}$ – $58^{\circ}$ N,  $100^{\circ}$ – $70^{\circ}$ W), and the southwestern United States (SWUS) ( $30^{\circ}$ – $40^{\circ}$ N,  $120^{\circ}$ – $105^{\circ}$ W). These five regions correspond to the five boxes in Fig. 7. As shown in Fig. 9a, the MME regional SAT anomalies capture distinct regional warming or cooling centers in the observations but differ in amplitude. The areal SAT anomalies in the RFE exhibit a large spread among the 27 (26) ensemble members, ranging from  $-1.67$  to  $0.14$  ( $-2.15$  to  $-0.62$ ) for CMIP5 (CMIP6) (Fig. 9a). In the CMIP5 (CMIP6) ensemble mean, winter regional SAT anomalies over NNA ranged from  $-0.61$  to  $1.54$  (0 to 1.41). However, the uncertainty

of areal SAT anomalies over MSA, GLNA, and SWUS are relatively small compared to the aforementioned two regions, as most model members produce consistent regional SAT anomalies (Fig. 9a). Additionally, an explicit simulation bias is observed in RFE, with prominent increases in SAT anomalies of  $-1.04^{\circ}$  and  $-1.17^{\circ}$ C for the CMIP5 and CMIP6 MME, respectively, compared to an observed value of  $-0.96$ . In NNA, the simulation of CMIP5 and CMIP6 MME is significantly overestimated, with values of  $0.54^{\circ}$  and  $0.54^{\circ}$ C, respectively, compared to only  $0.01^{\circ}$ C in observation.

The above results indicate that there are considerable divergences of the simulated SAT anomalies in the RFE and NNA regions. A question arises as to what factors are responsible for the intermodel diversity and overestimation of areal SAT anomalies in these two regions. Previous studies have demonstrated that WP-related circulation anomalies influence regional climate mainly through the thermal advective processes (Linkin and Nigam 2008; Lim and Kim 2013; Baxter and Nigam 2015). In addition, as has been mentioned above, the amplitudes of the WPnl are overestimated by most of the CMIP5 and CMIP6 models. Indeed, changes in circulation may affect the meridional temperature gradient via modulating the

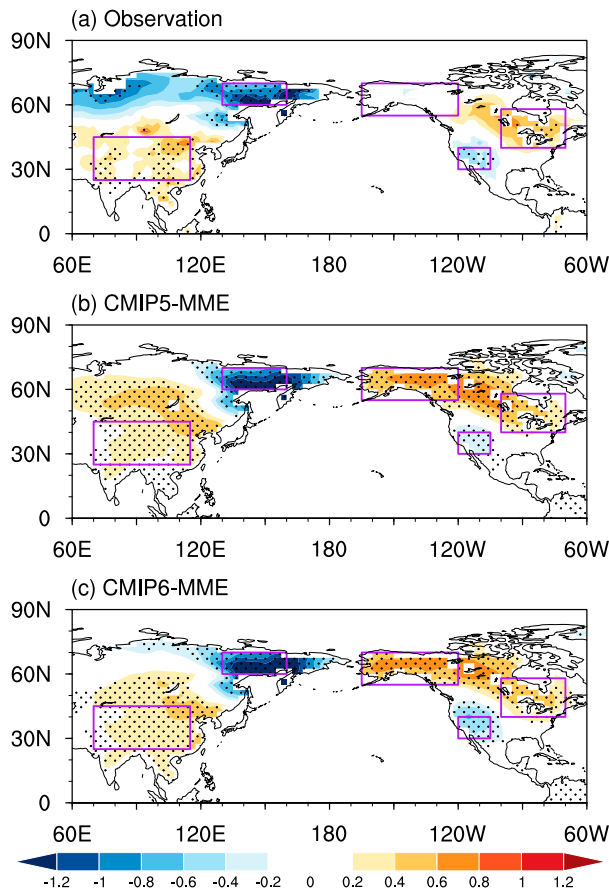


FIG. 7. Surface air temperature anomalies (shading; units:  $^{\circ}\text{C}$ ) regressed on the normalized WPIs in (a) observation and (b) CMIP5 and (c) CMIP6 historical simulation MMEs for 1950–2005. The boxes represent the corresponding five geographical areas: the Russian Far East region (RFE;  $60^{\circ}$ – $70^{\circ}\text{N}$ ,  $130^{\circ}$ – $160^{\circ}\text{E}$ ), midlatitude southern Asia (MSA;  $25^{\circ}$ – $45^{\circ}\text{N}$ ,  $70^{\circ}$ – $115^{\circ}\text{E}$ ), northwestern North America (NWN;  $55^{\circ}$ – $70^{\circ}\text{N}$ ,  $165^{\circ}$ – $120^{\circ}\text{W}$ ), the Great Lakes of North America (GLNA;  $40^{\circ}$ – $58^{\circ}\text{N}$ ,  $100^{\circ}$ – $70^{\circ}\text{W}$ ), and the southwestern United States (SWUS;  $30^{\circ}$ – $40^{\circ}\text{N}$ ,  $120^{\circ}$ – $105^{\circ}\text{W}$ ).

strength of the meridional advection. With this in mind, we hypothesize that the overestimated SAT anomalies over the RFE and NWN may be attributed to the performance of the models in capturing the WPnI. Hence, we first examine the link between the WP-related 850-hPa regional meridional wind anomalies and areal SAT anomalies over the RFE and NWN regions (Figs. 10a,b). It is clear that the models that produce strong northerly (southerly) wind anomalies over the RFE (NWN) tend to be accompanied by anomalous cooling (warming) SAT and vice versa. Specifically, the correlation coefficients between the CMIP5 and CMIP6 variables in Figs. 10a and 10b are 0.56 (0.43) and 0.73 (0.77), both significant at the 95% confidence level. This indicates that the regional SAT anomalies simulations are closely related to the regional meridional wind anomalies. In particular, stronger northerly (southerly) wind anomalies contribute to larger

negative (positive) SAT anomalies via bringing more cold (warm) air from higher (lower) latitude. Furthermore, Figs. 10c and 10d depict a scatterplot between the WPnI amplitude and the meridional wind anomalies in the 850-hPa region over RFE (NWN) in the CMIP5 and CMIP6 models. There is a significant correlation coefficient between the two variables, showing a synergistic association. Therefore, this suggests that the deviation of the models in reproducing the strength of SAT anomalies in RFE and NWN is closely related to the spread of the models in simulating the WPnI amplitude.

#### b. Intermodel differences in areal precipitation anomalies

To validate the ability of the climate models to simulate the WP-related precipitations anomalies, we first perform a comparison between the observations and model ensembles. Figure 11 displays regression maps of winter precipitation anomalies upon the WP indices for the observations and the ensemble means of the CMIP5 and CMIP6. In general, the MME can approximately reproduce the observed precipitation anomaly pattern. For instance, both CMIP5 and CMIP6 MME can reasonably reproduce the positive precipitation anomalies over the Southeast Asia coastal region and southeast North America, and the negative precipitation anomalies over the coastal region of northeastern Asia (Figs. 11b,c). However, a notable bias exists in western and central Siberia with distinctly overestimated negative precipitation anomalies there (Figs. 11b,c).

By focusing on the EU and NA regional precipitation simulations, Figs. 8c and 8d show the skill score of CMIP5 and CMIP6 models in reproducing the precipitation anomalies related to the WP. We find that the CMIP5 and CMIP6 models' precipitation simulations are not as good as for the SAT simulations, with a range from 0.13 to 0.48 (0.16 to 0.50) in CMIP5 (CMIP6) models in the EU region. Likewise, for the NA region, the skill scores range from 0.05 to 0.51 (0.06 to 0.38) in CMIP5 (CMIP6) models. The median and MMM skill scores in CMIP6 (0.33 and 0.32) are slightly improved compared to CMIP5 (0.31 and 0.30) (Fig. 8c), and the 0.02 incremental MMM skill scores is statistically significant above the 95% confidence level according to the bootstrap test. That is, the CMIP6 models perform relatively well in EU precipitation anomalies simulation. Conversely, the CMIP5 models are better than the CMIP6 models for precipitation simulations in North America (Fig. 8d).

Take a quantitative comparison of the WP-related precipitation anomalies over the six selected critical regions: northwestern Eurasia (NWEA;  $50^{\circ}$ – $70^{\circ}\text{N}$ ,  $70^{\circ}$ – $115^{\circ}\text{E}$ ), the coastal areas of northeastern Asia (Coastal-NEA;  $55^{\circ}$ – $65^{\circ}\text{N}$ ,  $135^{\circ}$ – $155^{\circ}\text{E}$ ), midlatitude Southeast Asia (Mid-SEA;  $25^{\circ}$ – $40^{\circ}\text{N}$ ,  $105^{\circ}$ – $120^{\circ}\text{E}$ ), the northwestern North America (NWN;  $60^{\circ}$ – $70^{\circ}\text{N}$ ,  $155^{\circ}$ – $120^{\circ}\text{W}$ ), midlatitude Canada (Mid-Canada;  $45^{\circ}$ – $65^{\circ}\text{N}$ ,  $120^{\circ}$ – $95^{\circ}\text{W}$ ), and southeast North America (SENA;  $30^{\circ}$ – $40^{\circ}\text{N}$ ,  $95^{\circ}$ – $80^{\circ}$ ). These six regions are outlined in Figs. 11a–c. Changes in the magnitude of areal precipitation anomalies conspicuously vary among models (Fig. 9b). Specifically, there exist large spreads among models in representing the WP-related areal precipitation anomalies over Mid-SEA, NWN, and SENA, with values within  $-0.23$  to  $0.51$  cm ( $-0.13$  to  $0.68$  cm),  $-0.54$  to  $0.58$  cm ( $-0.16$  to  $0.32$  cm), and  $-0.38$  to  $0.91$  cm

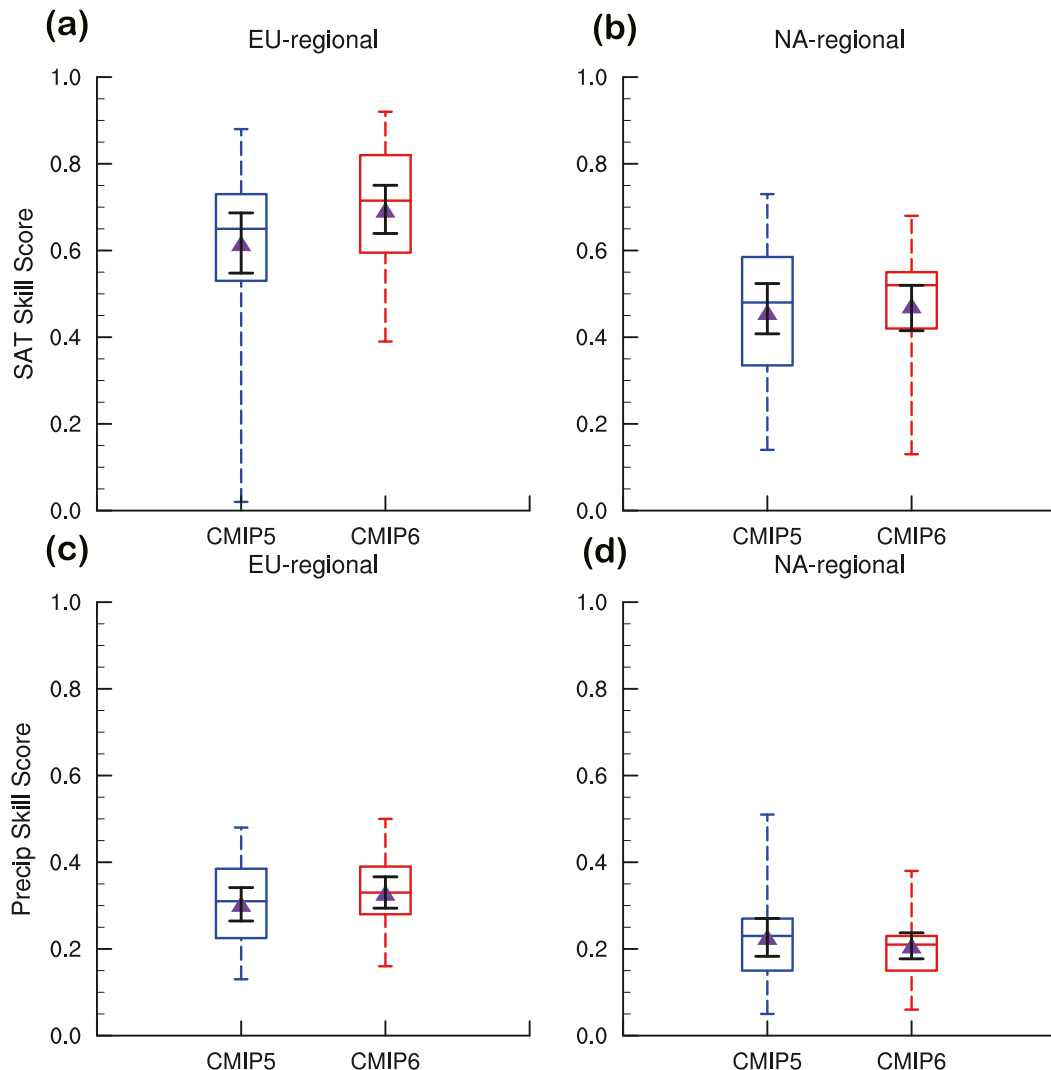


FIG. 8. Comparison of Eurasia (EU; 20°–80°N, 60°E–180°) and North America (NA; 20°–80°N, 160°–60°W) regional (a),(b) SAT and (c),(d) precipitation model simulation skill score in CMIP models. The blue boxes are for the CMIP5 historical simulations with a purple triangle indicating the average skill score of the submodels. The red boxes are for the CMIP6 historical simulations. The error bars overlaid on the multimodel mean (i.e., the purple triangle) represent the 95% confidence level determined by a bootstrap test.

(−0.03 to 1.11 cm) for CMIP5 (CMIP6) ensembles (Fig. 9b). This can also be intuitively deduced from the error bars, which are determined by bootstrap confidence levels, indicating greater intermodel variability (Fig. 9b). Meanwhile, compared with the observed precipitation anomalies, the MMEs of CMIP5 and CMIP6 are underestimated over these three regions (Fig. 9b), where the increments of MMM for CMIP6 compared to CMIP5 in the Central East and SENA regions are 0.04 and 0.056, respectively, which are greater than the 97.5% quantile of 0.035 and 0.053, indicating statistical significance above the 95% confidence level. Additionally, a smaller range of areal precipitation anomalies uncertainties are perceived over NWEA, Coastal-NEA, and Mid-Canada compared to the aforementioned three regions (Fig. 9b). There is a particularly prominent consistency among CMIP5 and

CMIP6 models for NWEA anomalous precipitation (Fig. 9b) as well as significant overestimation of precipitation anomalies (Figs. 11b,c).

In the following, we examine the possible factors leading to the large overestimated negative precipitation anomalies in western and central Siberia (Figs. 11b,c). We speculate that the overestimation of the precipitation anomalies might be partly related to the models' biases in the simulation of the climatological precipitation there. Figures 12a and 12b show the difference in the precipitation climatology between CMIP5 (CMIP6) models and observations. It is clear that almost all the models in the CMIP5 and CMIP6 show an overestimation of the precipitation climatology. We have also examined the connection of the WP-related precipitation anomalies in western and central Siberia with

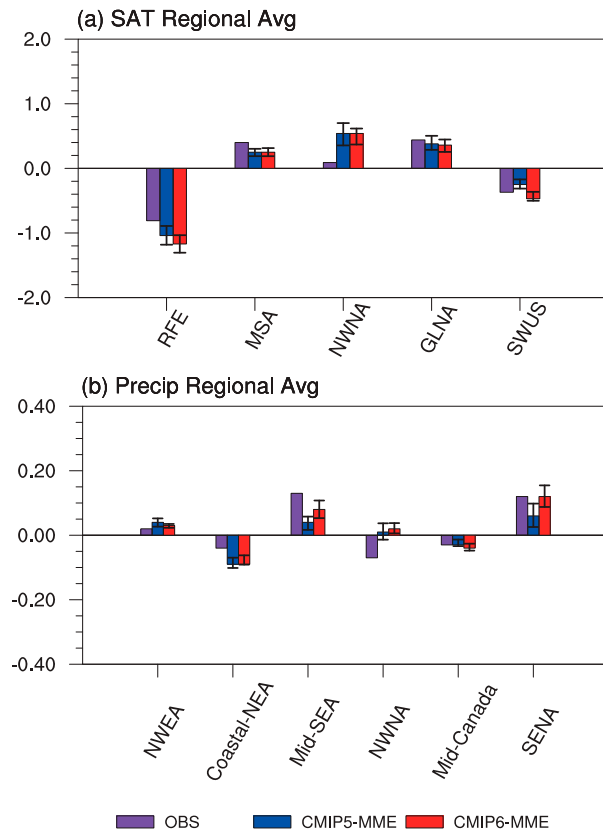


FIG. 9. Comparison of the regional (a) surface air temperature (SAT; units: °C) and (b) precipitation (Precip; units: cm) anomalies among observations (purple bars), CMIP5 MME of historical simulations (blue bars), and CMIP6 MME of historical simulations (red bars). The error bars overlaid on the multimodel mean represents the 95% confidence level determined by a bootstrap test.

the precipitation climatology there (Figs. 12c,d). The correlation coefficients between the WP-related precipitation anomalies and the model simulated precipitation climatology over western and central Siberia are 0.67 and 0.45 among the CMIP5 and CMIP6 models (Figs. 12c,d), both significant at the 95% confidence level. This suggests that the ability of the current models in simulating the WP-related precipitation anomalies over western and central Siberia is partly related to the models' performance in reproducing the precipitation climatology. Intermodel diversity in the simulation of the WP-related precipitation anomalies is larger over SENA compared to that over mid-Canada. The intermodel spreads of WP-related precipitation anomalies are partly related to the performance of the models in capturing the mean precipitation of the different regions (not shown).

#### c. Connection of the WP with the AO in the CMIP5 and CMIP6 models

The above sections have disclosed significant biases of the WP associated climate impacts. Here, we would like to explore more in depth the possible explanations for intermodel discrepancies

in WP-related climate impacts. As has been mentioned in section 3, the north region of the WP pattern is visibly overestimated in both CMIP5 and CMIP6 MME, which shares a striking similar spatial pattern with the AO (Thompson and Wallace 1998 2000) (Figs. 1b,c). AO is the dominant mode of atmospheric circulation anomalies in the extratropics of the Northern Hemisphere, with variability on multiple time scales from intraseasonal to multidecadal (Thompson and Wallace 1998 2000). Moreover, broad studies have demonstrated that the AO can significantly influence the climate over Northern Hemisphere, especially over Eurasia and North America (e.g., Chen et al. 2005, 2018a, 2018b; Jeong and Ho 2005; Park et al. 2011; Cheung et al. 2012; Kim and Ahn 2012; Woo et al. 2012; Choi et al. 2013; He et al. 2017; Huang et al. 2017; Chen and Song 2018 2019; Gong et al. 2018, 2019). Thus, it is reasonable to speculate that the performance of the coupled models in reproducing the WP-related climatic influences may be affected by the ability of the models in capturing the WP–AO connections.

Figure 13 displays the correlation coefficients between the WP and AO indices among individual CMIP5 and CMIP6 models. In the observation, WP has nearly no relation with the AO, suggesting that WP and AO are independent climate modes. However, both the CMIP5 and CMIP6 MMEs overestimate the connection between the WP and AO, attributing to many models produce a significant connection between them. In the following, we separate the models into WP–AO “high correlation” (HC) and “low correlation” (LC) groups based on the criterion that whether the correlation coefficients are significant at 90% confidence level or not. Based on this criterion, 16 models in CMIP5 (i.e., BCC-CSM1.1, BCC-CSM1.1.M, BNU-ESM, CMCC-CM, CSIRO-Mk3.6.0, FIO-ESM, GFDL CM3, GFDL-ESM2G, GFDL-ESM2M, GISS-E2-H, GISS-E2-R, IPSL-CM5A-LR, MIROC-ESM-CHEM, MIROC5, NorESM1-M, NorESM1-ME) and 13 models in CMIP6 (i.e., ACCESS-CM2, ACCESS-ESM1-5, BCC-CSM2-MR, BCC-ESM1, CESM2, CESM2-WACCM, CMCC-CM2-SR5, E3SM-1-0, EC-Earth3, GFDL-ESM4, INM-CM5-0, IPSL-CM6A-LR, MIROC6) are selected as the HC groups, and the other 11 and 13 models are classified into the LC groups in CMIP5 and CMIP6, respectively.

Figure 14 shows the WP-related SAT anomalies for the ensemble means of the HC and LC groups in CMIP5 and CMIP6. We find that the spatial distribution of the SAT anomalies for the LC model group (Figs. 14b,d) bears a closer resemblance to the observed result (Fig. 7a) as compared to the HC model group (Figs. 14a,c), particularly over Eurasia. We have calculated the spatial correlation coefficients (CCs) of the SAT anomalies over the EU between the HC and LC groups with the observation in CMIP5 and CMIP6. The LC group MME simulation patterns well match with the observations, with the CMIP6 (CMIP5) CCs reaching 0.89 (0.78), much higher than that in the HC group 0.60 (0.58) (Fig. 14). In contrast, compared with the HC group (Figs. 14a,c), the improvement in the simulation of the spatial distribution of SAT anomalies in NA is relatively weak in the CMIP6 (CMIP5) LC group (Figs. 14b,d).

Likewise, the spatial pattern of the precipitation anomalies in the LC group (Figs. 15b,d) also matches better with

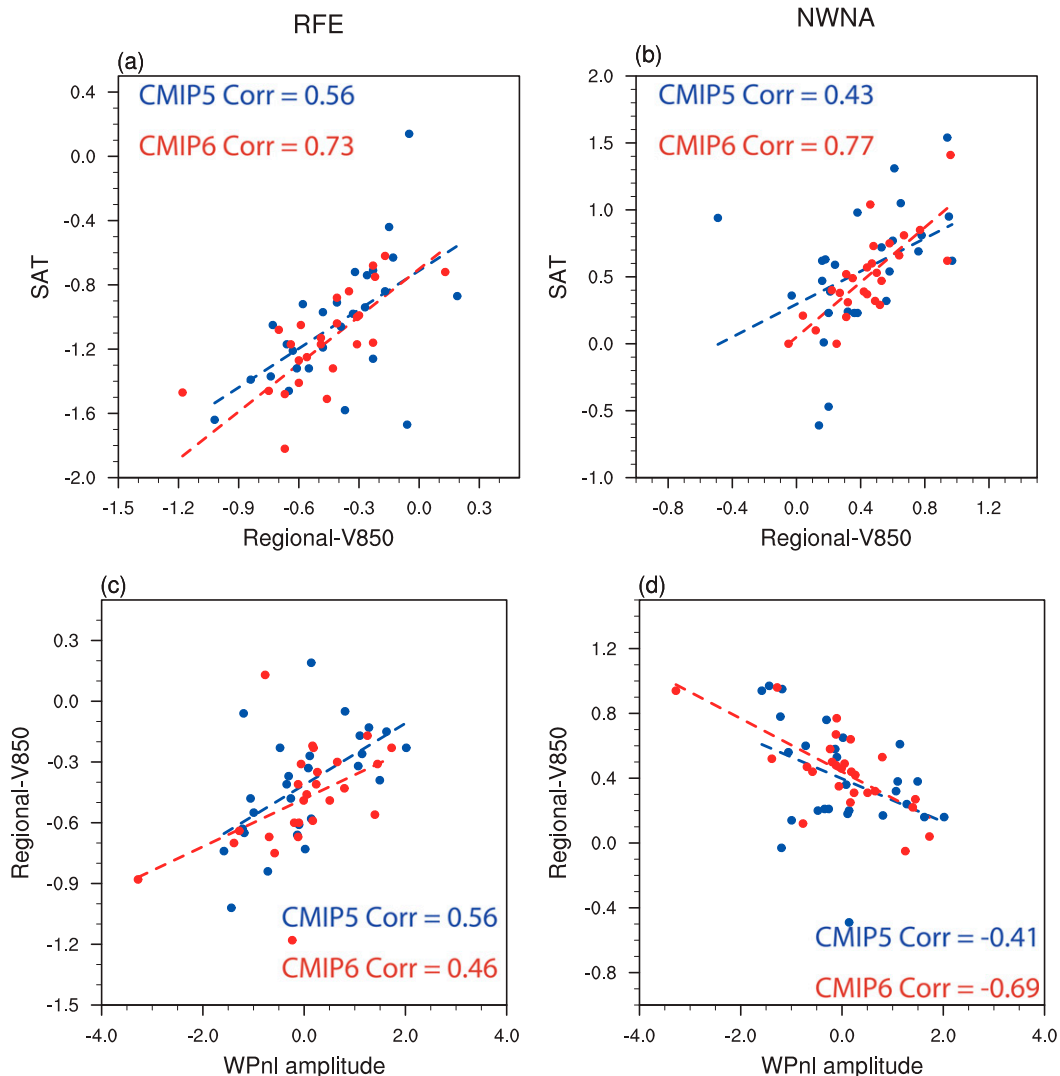


FIG. 10. Relationship of the WP-related areal average of 850-hPa meridional wind vs the regional WP SAT anomalies over (a) RFE (60°–70°N, 130°–160°E) and (b) NWNA (55°–70°N; 165°–120°W) in CMIP5 (blue dots) and CMIP6 (red dots). (c),(d) As in (a) and (b), but for the amplitude of WPnI and the 850-hPa meridional wind anomalies of WP over RFE and NWNA.

the observation (Fig. 11a) compared to the HC group (Figs. 15a,c). A closer inspection shows that the overestimation of precipitation anomalies in the Siberian region was not present in the LC group, but was still present in the HC group. Meanwhile, the LC group has improved the simulation of anomalous precipitation in NA, especially for negative precipitation anomalies in the southeastern United States, and positive precipitation anomalies in northwestern Alaska and the central Canadian Plains. In this regard, it can be concluded that there are notable improvements in the simulation of WP-related SAT and precipitation anomalies, especially for the WP–AO LC group models in the EU region. Hence, this evidence verifies our speculation about the relationship of the coupled models' performance in reproducing the WP-related climate

anomalies with the capability of the models in capturing the WP–AO connections.

## 5. Summary and discussion

The present study assesses and compares the performances of CMIP5 and CMIP6 climate models in simulating the horizontal and vertical structures, dominant frequency, and climatic effects of winter WP. The MME patterns of both the CMIP5 and CMIP6 models capture the observed WP well, presenting a north–south dipole pattern in the mid- to high latitudes of the North Pacific. The high latitudes of the North Pacific, on the other hand, show a significant overestimation in reproducing the northern lobe of the WP. The MME captures well the equivalent barotropic dipole structure of the



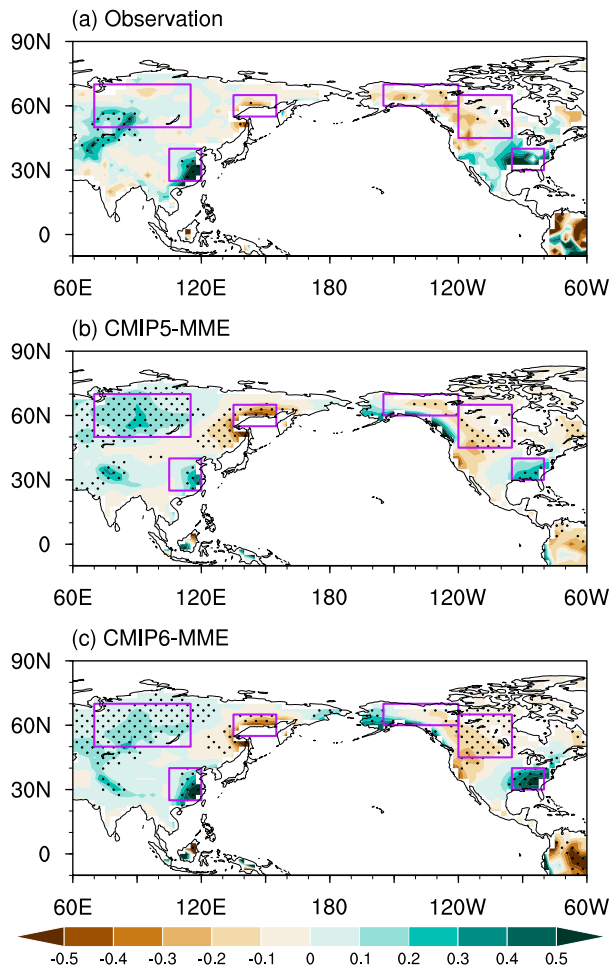


FIG. 11. Precipitation anomalies (shading; units:  $\text{kg m}^{-2} \text{day}^{-1}$ ) regressed on the normalized WPIs in (a) observations and (b) CMIP5 and (c) CMIP6 historical simulations MME for 1950–2005. The boxes represent the six geographical areas: northwestern Eurasia (NWEA;  $50^{\circ}$ – $70^{\circ}\text{N}$ ,  $70^{\circ}$ – $115^{\circ}\text{E}$ ), the coastal region of northeastern Asia (Coastal-NEA;  $55^{\circ}$ – $65^{\circ}\text{N}$ ,  $135^{\circ}$ – $155^{\circ}\text{E}$ ), midlatitude southeastern Asia (Mid-SEA;  $25^{\circ}$ – $40^{\circ}\text{N}$ ,  $105^{\circ}$ – $120^{\circ}\text{E}$ ), northwestern North America (NWNNA;  $60^{\circ}$ – $70^{\circ}\text{N}$ ,  $155^{\circ}$ – $120^{\circ}\text{W}$ ), midlatitude Canada (Mid-Canada;  $45^{\circ}$ – $65^{\circ}\text{N}$ ,  $120^{\circ}$ – $95^{\circ}\text{W}$ ), and southeastern North America (SENA;  $30^{\circ}$ – $40^{\circ}\text{N}$ ,  $95^{\circ}$ – $80^{\circ}\text{W}$ ).

geopotential height of the WP over the North Pacific. A quantitative comparison of the simulated amplitudes of WPnI and WPsl reveals that the WPnI amplitude simulations exhibit consistent intensified deviations in the CMIP5 and CMIP6 MME, while there is no consensus on the WPsl amplitude. Additionally, individual model portrayals vary primarily in the WPnI amplitude. The maximum positive Z500 anomalies over the North Pacific locates to the east, while the minimum negative Z500 anomalies in the MME moves to the west. In terms of temporal characteristics, the spectral analysis shows that most models reproduce significant interannual power spectra presented in the observations, with relatively large amplitudes. At the same time, the models generally overestimate the decadal variation of the WP. Overall, compared to the CMIP5

model, historical simulations of CMIP6 are found to 1) better simulate the spatial features of the WP, with smaller spreads in the pattern correlation and normalized standard deviation of the spatial pattern, 2) improve in reproducing longitudinal positions of the WP, and 3) improve in capturing the interannual variations of the WP.

Another primary goal of the current study is to examine whether the current climate models can simulate the climatic anomalies over Eurasia and North America associated with WP. Investigations of the SAT and precipitation anomalies reproduced by the MME indicate that the model reasonably well describes the observed distribution of air temperature and precipitation anomalies. However, the MME largely overestimates the surface air temperature anomalies in the RFE and NWNNA, as well as overestimates the precipitation anomalies in Siberia. The scatterplots between the mean SAT anomalies and the mean 850-hPa meridional wind anomalies in the two regions confirm that the performance of the CMIP5 and CMIP6 models in simulating the SAT anomalies in the RFE and the NWNNA is attributed to the ability of models to reproduce the WPnI amplitude. In addition, by analyzing the relationship between precipitation climatology and WP-related anomalous precipitation in the Siberian region, it is found that differences in the simulation of WP-related precipitation anomalies in the Siberian region are due partly to a corresponding overestimation of precipitation climatology. Most of the CMIP5 and CMIP6 models overestimate the WP–AO connection. We find that the WP–AO LC group performs better compared to the HC group in reproducing the WP-related SAT and precipitation anomalies, especially over Eurasia.

As has been mentioned above, there exist large differences in the WP–AO relation between the observation and CMIP5/CMIP6 models. In particular, in the observation, the WP has a weak relation with the AO (Fig. 1a). By contrast, both the CMIP5 and CMIP6 MME produce a close WP–AO connection (Figs. 1b,c). It is noted that AO is considered to be an important intrinsic atmospheric mode, and studies have demonstrated that the interaction between the synoptic-scale eddy activity (also known as storm track) and low-frequency mean flow plays a crucial role in the formation and maintenance of AO-related monthly mean circulation anomalies over the mid- to high-latitude North Pacific (Hartmann and Lo 1998; Lorenz and Hartmann 2003; Thompson et al. 2003; Chen et al. 2014). This suggests, to a certain extent, that the model's simulation of the WP–AO relationship may be related to the model's ability to simulate the North Pacific storm track. Several studies (Ulbrich et al. 2009; Chang et al. 2012; Zappa et al. 2014; Yang et al. 2018; Harvey et al. 2020) have shown that the position of the North Pacific storm track is found to be shifted northward in the CMIP5 and CMIP6 models than the observed. The northward movement of the North Pacific storm track in the CMIP5/CMIP6 may provide a favorable condition in connecting the atmospheric anomalies over high latitudes and midlatitudes via wave–mean flow interaction, and thus may contribute to a closer AO–WP relation (Lau 1988; Lau and Nath 1991; Chen et al. 2014). The detailed factors responsible

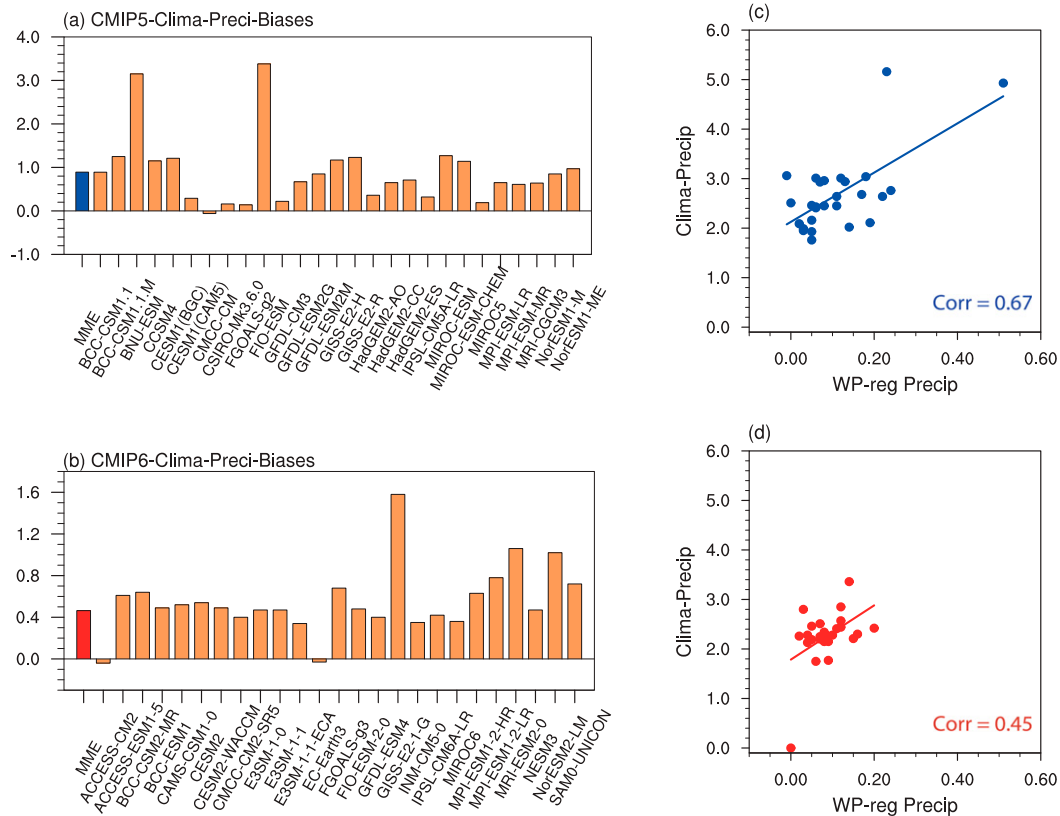


FIG. 12. Biases in the areal climatological precipitation (units: cm) of (a) CMIP5 and (b) CMIP6 models and their ensemble means. Biases are defined as the climatological precipitation over northwestern Eurasia (NWEA; 50°–70°N, 70°–115°E) in model simulations minus those in observations during 1950–2005. (c),(d) Scatterplots of the areal average of precipitation anomalies with respect to the WP over NWEA vs the corresponding areal precipitation climatology in CMIP5 and CMIP6, respectively.

for the large diversity of the WP–AO relation in the CMIP models remain to be explored.

This study detected the spatial pattern of WP and its climatic impacts based on the observational and reanalysis data from 1950 to 2005. One may doubt whether WP and its associated climatic anomalies can still be obtained over longer or shorter time periods. To substantiate the above results, we have examined the spatial pattern of WP and the corresponding climatic anomalies for the periods of 1950–2015 and 1979–2019, respectively (not shown). Results reveal that the spatial pattern of WP and its climatic impacts were consistent across the three periods. Thus, the results obtained in this study are not sensitive to the selection of the analysis period.

The North Pacific Oscillation (NPO) is the second EOF mode of the sea level pressure (SLP) anomalies over the North Pacific (Rogers 1981; Walker and Bliss 1932). Several studies have suggested that NPO can be considered as a surface signature of the WP (Linkin and Nigam 2008; Nigam and Baxter 2015). Hence, one may want to know whether CMIP6 also shows an improvement in the simulation of the NPO. To address this issue, we defined the NPO index on the basis of projection method similar to the definition of the WP index. In particular, we performed an EOF analysis to the observed and

detrended monthly SLP anomalies over the North Pacific (20°–85°N, 120°E–120°W) following Linkin and Nigam (2008). Then, the EOF2 stands for the NPO pattern as generally defined in previous studies (Linkin and Nigam 2008; Nigam and Baxter 2015). Finally, the observed NPO index is obtained by projecting the observed and detrended SLP anomalies onto the aforementioned EOF2. Similarly, the NPO indices in the CMIP models are obtained by projecting the simulated SLP anomalies onto the observed EOF2 of SLP. The monthly WP and NPO time series are presented in (Fig. S1 in the online supplemental material), with a correlation coefficient of 0.7 between them for the period 1950–2005. This indicates that the WP and NPO share about 49% of the common variance. Thus, the NPO is not totally identical to the WP.

To further examine simulation of the NPO, a more in-depth investigation of the NPO pattern in CMIP models was carried out. Figure S2 shows spatial patterns of SLP and 850-hPa wind anomalies in association with the winter NPO in the observation, CMIP5 MME, and CMIP6 MME over the period of 1950–2005. The NPO features a meridional dipole structure of SLP anomalies in the extratropical North Pacific. The CMIP5 and CMIP6 MMEs well reproduced the spatial pattern of the observed NPO. In addition, the amplitude of the southern center

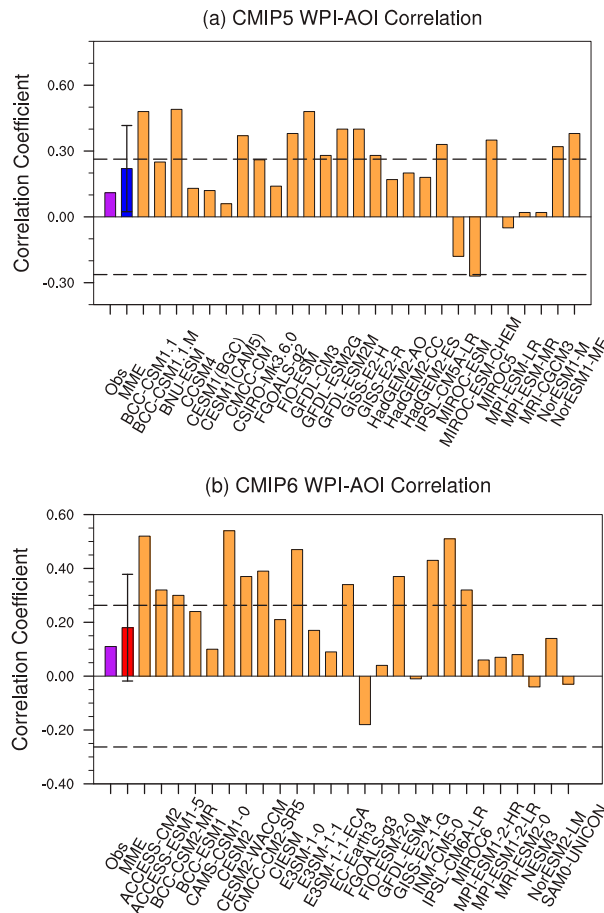


FIG. 13. The correlation coefficients between the WP and AO index in observation and among (a) CMIP5 and (b) CMIP6 models. The corresponding multimodel means and their uncertainties based on one standard deviation are indicated by the blue (red) bars with error bars. The purple bars denote the observed correlation coefficients of WP–AO. The dashed lines indicate the 95% confidence level.

of the winter NPO is slightly weaker in both CMIP5 and CMIP6 (Figs. S2b,c) compared to the observation (Fig. S2a), while the latter shows an improvement (Fig. S2c). A Taylor diagram was further constructed to objectively estimate how well the CMIP5 and CMIP6 models reproduce the observed NPO in the extratropical North Pacific (20°–80°N, 120°E–120°W; Fig. S3a). The pattern correlation coefficients between CMIP models and the observations are above 0.85. The intermodal spreads of the normalized standard deviation are reduced from the CMIP5 (0.8–1.83) to CMIP6 (0.95–1.73). The pattern correlation for the CMIP6 MME is 0.98, larger than that for the CMIP5 MME ( $r = 0.97$ ) (Fig. S3a). Moreover, the normalized standard deviation is 1.19 for the CMIP6 MME, less than that for the CMIP5 MME (1.22) (Fig. S3a).

Figure S3b further shows a box-and-whisker plot of skill scores for CMIP5 and CMIP6 models for the NPO spatial pattern. The CMIP6 models exhibit less dispersion of skill scores than the CMIP5 models. The skill score ranges from 0.64

to 0.96 in the CMIP5 models, while it ranges from 0.71 to 0.96 in the CMIP6 models (Fig. S3b). For the multimodel mean, the skill scores of the winter NPO in CMIP6 (0.88) is higher than that for the CMIP5 (0.85) (Fig. S3b). Therefore, the above evidence indicates an improvement in the CMIP6 models in simulating the winter NPO.

It is worth mentioning that the nature of WP dynamics not only depends on external forcings in the tropics and extratropics but is also regarded as an intrinsic atmospheric circulation variability. Recently, many studies have reported that internal variability is one of the main contributors to the model simulation uncertainties (e.g., Deser et al. 2012, 2014, 2017; Bengtsson and Hodges 2019; Zheng et al. 2018; Beobide-Arsuaga et al. 2021). Issues related to uncertainties in internal variability can be addressed based on large ensemble simulations, which provide new insight into uncertainties due to internal variability versus model differences (Deser et al. 2020). In this study, we selected only one ensemble member in each model, as only one member run is available for many of the models we employed. This can avoid biasing the results toward the physics of any given model. To quantify the uncertainty in the outcomes across models, we have examined two representative models from CMIP5 (MIROC5 and ACCESS-CM2) and another two from CMIP6 (CESM1-CAM5 and HadGEM2-ES), with relatively high and low spatial pattern correlation coefficients according to Taylor diagrams, respectively. Despite the different simulation capabilities, the intermember differences in the above models are relatively small (not shown). In addition, there is no overlap between the multiple members of the different models. Thus, this excludes the possibility that differences in the results are mainly due to uncertainty in the sample selection.

In this study, an improvement in representing the dominant periodicity of the WP emerged in CMIP6. Generally, there is a consensus that external forcing such as tropical and extratropical sea surface temperature anomalies (Horel and Wallace 1981; Kodera 1998; Koide and Kodera 1999; Hirose et al. 2009; Frankignoul et al. 2011), snow cover over Eurasia (Nakamura et al. 2015), and Arctic sea ice (Linkin and Nigam 2008; Yuan et al. 2015; Xu and Fan 2020) play a role in the formation and maintenance of the WP. An observational study (Aru et al. 2021) also revealed that the ~5-yr periodicity of the WP is associated with ENSO. Recent studies suggested that CMIP6 models perform better in simulating Arctic sea ice and ENSO-related characteristics compared to the CMIP5 models (Notz and SIMIP Community 2020; Long et al. 2021; Beobide-Arsuaga et al. 2021), which may hint at the improved reproducibility of WP periodicity. More attention should be paid to explore the specific physical processes that contribute to the better performance of the CMIP6 in reproducing dominant periodicity of WP.

Previous studies have reported that WP has an impact on the stratospheric climate (e.g., Limpasuvan et al. 2005; Orsolini et al. 2009; Nishii et al. 2010, 2011; Woollings et al. 2010; Dai and Tan 2016). The negative (positive) phase of the WP tends to lead to stratospheric cooling (warming) through modulation of stratospheric planetary waves, suggesting that the WP may

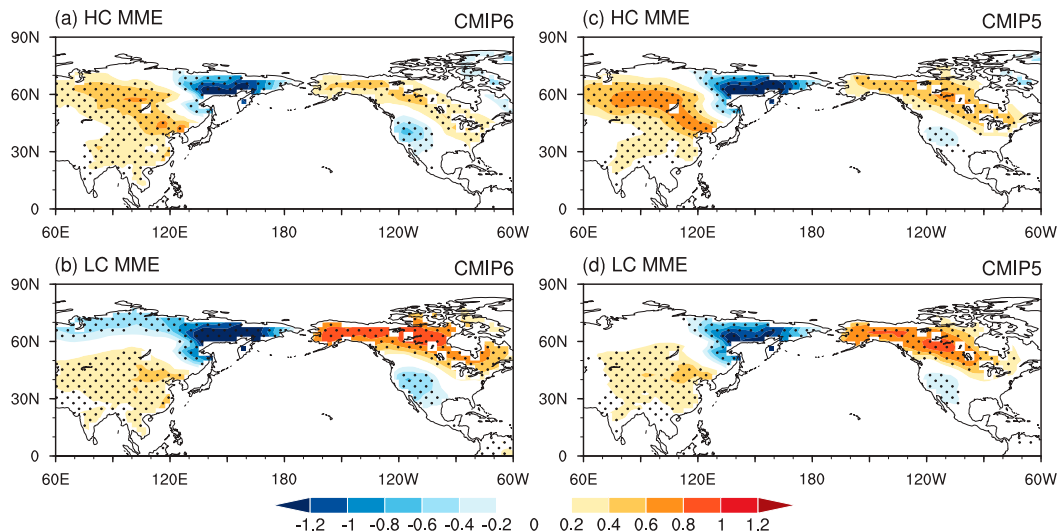


FIG. 14. The DJF-mean surface air temperature (SAT; units:  $^{\circ}\text{C}$ ) anomalies obtained through regressing upon the CMIP6 MME (a) HC group and (b) LC group of WP and AO during 1950–2005 historical simulations. (c),(d) As in (a) and (b), but for the CMIP5 MME. The anomalies that are significantly different from zero at the 95% confidence level are stippled.

serve as an essential precursor to stratospheric sudden warmings (SSWs). However, an explicit examination of the WP–SSW relationship requires daily mean data. We have preliminary analyzed latitude–height cross section of winter WP-related zonal mean air temperature anomalies (Figs. S4 and S5). In the observation, strong warming signals are seen over high latitude above 300 hPa during positive phase of WP. Almost all the CMIP5 models analyzed in this study can capture the main features of observed zonal mean air temperature anomalies related to the WP (Fig. S4). In contrast, many CMIP6 models fail to simulate the observed characteristic of air temperature anomalies at the stratosphere (Fig. S5).

Further investigations are needed to examine why CMIP6 models have limitations in simulating the WP-related air temperature anomalies at the stratosphere.

This study finds that there exist large spreads in simulating the spatial structure of the WP across the CMIP models. Previous studies have interpreted the WP as a result of kinetic energy (KE) conversion and baroclinic conversion of available potential energy (APE) and the feedback forcing by transient eddies (Tanaka et al. 2016). Sung et al. (2019) demonstrated that spatial change of the NPO (i.e., the lower-tropospheric footprint of the WP) may have a connection to the mean baroclinicity, which can significantly affect the zonal position of

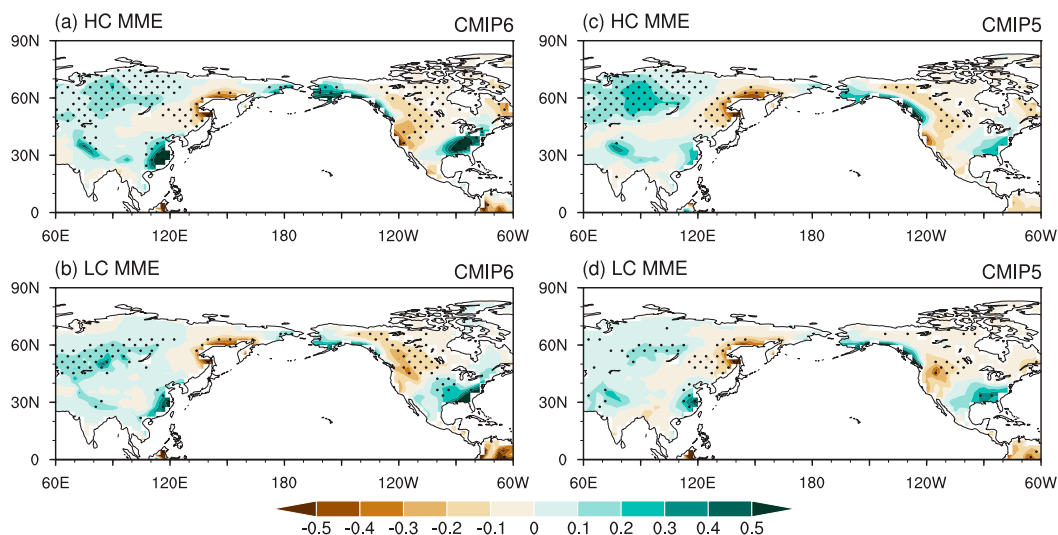


FIG. 15. (a)–(d) As in Figs. 14a–d, respectively, but for the DJF-mean precipitation (units: cm) anomalies of HC group and LC group in CMIP5 and CMIP6.



the NPO through modulating the horizontal distribution of APE conversion. We first selected models with the westernmost and easternmost WP centers. Then, we investigated the energy conversion terms associated with the WP centers in terms of the energy of the different models. In the easternmost and westernmost WPsl and WPnl models, significant differences in the contributing KE transitions from the climatological background flow and the lower tropospheric baroclinicity were observed (not shown). Hence, it could conceivably be inferred that diversity in the simulation of the WP's spatial structure can be partly attributed to the differences in the simulated energetic properties of WP. Considering the limited length of this paper, we intend to further proceed with an in-depth discussion of this aspect in the near future.

**Acknowledgments.** We thank Editor Dr. Isla Ruth Simpson and three anonymous reviewers for their constructive suggestions, which helped to significantly improve the paper. This study was supported jointly by the National Natural Science Foundation of China (Grants 41961144025, 41721004, and 42175039), and the Chinese Academy of Sciences Key Research Program of Frontier Sciences (QYZDY-SSW-DQC024). The authors declare no potential conflict of interest.

#### REFERENCES

- Aru, H., S. Chen, and W. Chen, 2021: Comparisons of the different definitions of the western Pacific pattern and associated winter climate anomalies in Eurasia and North America. *Int. J. Climatol.*, **41**, 2840–2859, <https://doi.org/10.1002/joc.6993>.
- Austin, P. C., and J. V. Tu, 2004: Bootstrap methods for developing predictive models. *Amer. Stat.*, **58**, 131–137, <https://doi.org/10.1198/0003130043277>.
- Baxter, S., and S. Nigam, 2015: Key role of the North Pacific Oscillation–west Pacific pattern in generating the extreme 2013/14 North American winter. *J. Climate*, **28**, 8109–8117, <https://doi.org/10.1175/JCLI-D-14-00726.1>.
- Bengtsson, L., and K. I. Hodges, 2019: Can an ensemble climate simulation be used to separate climate change signals from internal unforced variability? *Climate Dyn.*, **52**, 3553–3573, <https://doi.org/10.1007/s00382-018-4343-8>.
- Beobide-Arsuaga, G., T. Bayr, A. Reintges, and M. Latif, 2021: Uncertainty of ENSO-amplitude projections in CMIP5 and CMIP6 models. *Climate Dyn.*, **56**, 3875–3888, <https://doi.org/10.1007/s00382-021-05673-4>.
- Blackmon, M. L., R. A. Madden, J. M. Wallace, and D. S. Gutzler, 1979: Geographical variations in the vertical structure of geopotential height fluctuations. *J. Atmos. Sci.*, **36**, 2450–2466, [https://doi.org/10.1175/1520-0469\(1979\)036<2450:GVTVS>2.0.CO;2](https://doi.org/10.1175/1520-0469(1979)036<2450:GVTVS>2.0.CO;2).
- Bonfils, C. J. W., B. D. Santer, T. J. Phillips, K. Marvel, L. R. Leung, C. Doutriaux, and A. Capotondi, 2015: Relative contributions of mean-state shifts and ENSO-driven variability to precipitation changes in a warming climate. *J. Climate*, **28**, 9997–10013, <https://doi.org/10.1175/JCLI-D-15-0341.1>.
- Chang, E. K. M., Y. Guo, and X. Xia, 2012: CMIP5 multimodel ensemble projection of storm track change under global warming. *J. Geophys. Res.*, **117**, D23118, <https://doi.org/10.1029/2012JD018578>.
- Chen, L., Y. Yu, and D.-Z. Sun, 2013: Cloud and water vapor feedbacks to the El Niño warming: Are they still biased in CMIP5 models? *J. Climate*, **26**, 4947–4961, <https://doi.org/10.1175/JCLI-D-12-00575.1>.
- Chen, S., and L. Song, 2018: The leading interannual variability modes of winter surface air temperature over Southeast Asia. *Climate Dyn.*, **52**, 4715–4734, <https://doi.org/10.1007/s00382-018-4406-x>.
- , and —, 2019: Recent strengthened impact of the winter Arctic Oscillation on the Southeast Asian surface air temperature variation. *Atmosphere*, **10**, 164, <https://doi.org/10.3390/atmos10040164>.
- , B. Yu, and W. Chen, 2014: An analysis on the physical process of the influence of AO on ENSO. *Climate Dyn.*, **42**, 973–989, <https://doi.org/10.1007/s00382-012-1654-z>.
- , R. Wu, and W. Chen, 2018a: A strengthened impact of November Arctic Oscillation on subsequent tropical Pacific sea surface temperature variation since the late-1970s. *Climate Dyn.*, **51**, 511–529, <https://doi.org/10.1007/s00382-017-3937-x>.
- , —, L. Song, and W. Chen, 2018b: Combined influence of the Arctic Oscillation and the Scandinavia pattern on spring surface air temperature variations over Eurasia. *J. Geophys. Res. Atmos.*, **123**, 9410–9429, <https://doi.org/10.1029/2018JD028685>.
- , —, W. Chen, and L. Song, 2019: Performance of the CMIP5 models in simulating the Arctic Oscillation during boreal spring. *Climate Dyn.*, **53**, 2083–2101, <https://doi.org/10.1007/s00382-019-04792-3>.
- , —, K. Hu, and B. Yu, 2020: Structure and dynamics of a springtime atmospheric wave train over the North Atlantic and Eurasia. *Climate Dyn.*, **54**, 5111–5126, <https://doi.org/10.1007/s00382-020-05274-7>.
- , B. Yu, R. Wu, W. Chen, and L. Song, 2021: The dominant North Pacific atmospheric circulation patterns and their relations to Pacific SSTs: Historical simulations and future projections in the IPCC AR6 models. *Climate Dyn.*, **56**, 701–725, <https://doi.org/10.1007/s00382-020-05501-1>.
- Chen, W., S. Yang, and R.-H. Huang, 2005: Relationship between stationary planetary wave activity and the East Asian winter monsoon. *J. Geophys. Res.*, **110**, D14110, <https://doi.org/10.1029/2004JD005669>.
- Chen, Z., B. Gan, L. Wu, and F. Jia, 2017: Pacific–North American teleconnection and North Pacific Oscillation: Historical simulation and future projection in CMIP5 models. *Climate Dyn.*, **50**, 4379–4403, <https://doi.org/10.1007/s00382-017-3881-9>.
- Cheung, H. H. N., and W. Zhou, 2016: Simple metrics for representing East Asian winter monsoon variability: Urals blocking and western Pacific teleconnection patterns. *Adv. Atmos. Sci.*, **33**, 695–705, <https://doi.org/10.1007/s00376-015-5204-6>.
- , —, H. Y. Mok, and M. C. Wu, 2012: Relationship between Ural–Siberian blocking and the East Asian winter monsoon in relation to the Arctic Oscillation and El Niño–Southern Oscillation. *J. Climate*, **25**, 4242–4257, <https://doi.org/10.1175/JCLI-D-11-00225.1>.
- Choi, K.-S., S.-D. Kang, and H.-D. Kim, 2013: Possible relationship between North Korean total rainfall and Arctic Oscillation in May. *Theor. Appl. Climatol.*, **112**, 483–494, <https://doi.org/10.1007/s00704-012-0738-3>.
- Dai, Y., and B. Tan, 2016: The western Pacific pattern precursor of major stratospheric sudden warmings and the ENSO modulation. *Environ. Res. Lett.*, **11**, 124032, <https://doi.org/10.1088/1748-9326/aa538a>.
- , and —, 2019: Two types of the western Pacific pattern, their climate impacts, and the ENSO modulations. *J. Climate*, **32**, 823–841, <https://doi.org/10.1175/JCLI-D-17-0618.1>.
- , S. B. Feldstein, B. Tan, and S. Lee, 2017: Formation mechanisms of the Pacific–North American teleconnection



- with and without its canonical tropical convection pattern. *J. Climate*, **30**, 3139–3155, <https://doi.org/10.1175/JCLI-D-16-0411.1>.
- Deser, C., A. Phillips, V. Bourdette, and H. Teng, 2012: Uncertainty in climate change projections: The role of internal variability. *Climate Dyn.*, **38**, 527–546, <https://doi.org/10.1007/s00382-010-0977-x>.
- , —, M. A. Alexander, and B. V. Smoliak, 2014: Projecting North American climate over the next 50 years: Uncertainty due to internal variability. *J. Climate*, **27**, 2271–2296, <https://doi.org/10.1175/JCLI-D-13-00451.1>.
- , I. R. Simpson, K. A. McKinnon, and A. S. Phillips, 2017: The Northern Hemisphere extratropical atmospheric circulation response to ENSO: How well do we know it and how do we evaluate models accordingly? *J. Climate*, **30**, 5059–5082, <https://doi.org/10.1175/JCLI-D-16-0844.1>.
- , and Coauthors, 2020: Insights from Earth system model initial-condition large ensembles and future prospects. *Nat. Climate Change*, **10**, 277–286, <https://doi.org/10.1038/s41558-020-0731-2>.
- Di Lorenzo, E., and Coauthors, 2010: Central Pacific El Niño and decadal climate change in the North Pacific Ocean. *Nat. Geosci.*, **3**, 762–765, <https://doi.org/10.1038/ngeo984>.
- Eyring, V., S. Bony, G. A. Meehl, C. A. Senior, B. Stevens, R. J. Stouffer, and K. E. Taylor, 2016: Overview of the Coupled Model Intercomparison Project Phase 6 (CMIP6) experimental design and organization. *Geosci. Model Dev.*, **9**, 1937–1958, <https://doi.org/10.5194/gmd-9-1937-2016>.
- Feldstein, S. B., and C. L. E. Franzke, 2017: Atmospheric teleconnection patterns. *Nonlinear and Stochastic Climate Dynamics*, C. Franzke and T. O’Kane, Eds., Cambridge University Press, 54–104, <https://doi.org/10.1017/9781316339251.004>.
- Frankignoul, C., N. Sennéchal, Y.-O. Kwon, and M. A. Alexander, 2011: Influence of the meridional shifts of the Kuroshio and the Oyashio Extensions on the atmospheric circulation. *J. Climate*, **24**, 762–777, <https://doi.org/10.1175/2010JCLI3731.1>.
- Furtado, J. C., E. Di Lorenzo, B. T. Anderson, and N. Schneider, 2012: Linkages between the North Pacific Oscillation and central tropical Pacific SSTs at low frequencies. *Climate Dyn.*, **39**, 2833–2846, <https://doi.org/10.1007/s00382-011-1245-4>.
- Gong, H., L. Wang, W. Chen, and D. Nath, 2018: Multidecadal fluctuation of the wintertime Arctic Oscillation pattern and its implication. *J. Climate*, **31**, 5595–5608, <https://doi.org/10.1175/JCLI-D-17-0530.1>.
- , —, and —, 2019: Multidecadal changes in the influence of the Arctic Oscillation on the East Asian surface air temperature in boreal winter. *Atmosphere*, **10**, 757, <https://doi.org/10.3390/atmos10120757>.
- Hartmann, D. L., and F. Lo, 1998: Wave-driven zonal flow vacillation in the Southern Hemisphere. *J. Atmos. Sci.*, **55**, 1303–1315, [https://doi.org/10.1175/1520-0469\(1998\)055<1303:WDZFVI>2.0.CO;2](https://doi.org/10.1175/1520-0469(1998)055<1303:WDZFVI>2.0.CO;2).
- Harvey, B. J., P. Cook, L. C. Shaffrey, and R. Schiemann, 2020: The response of the Northern Hemisphere storm tracks and jet streams to climate change in the CMIP3, CMIP5, and CMIP6 climate models. *J. Geophys. Res. Atmos.*, **125**, e2020JD032701, <https://doi.org/10.1029/2020JD032701>.
- He, S., Y. Gao, F. Li, H. Wang, and Y. He, 2017: Impact of Arctic Oscillation on the East Asian climate: A review. *Earth-Sci. Rev.*, **164**, 48–62, <https://doi.org/10.1016/j.earscirev.2016.10.014>.
- Hirose, N., K. Nishimura, and M. Yamamoto, 2009: Observational evidence of a warm ocean current preceding a winter teleconnection pattern in the northwestern Pacific. *Geophys. Res. Lett.*, **36**, L09705, <https://doi.org/10.1029/2009GL037448>.
- Hirota, N., Y. N. Takayabu, M. Watanabe, and M. Kimoto, 2011: Precipitation reproducibility over tropical oceans and its relationship to the double ITCZ problem in CMIP3 and MIROC5 climate models. *J. Climate*, **24**, 4859–4873, <https://doi.org/10.1175/2011JCLI4156.1>.
- Horel, J. D., and J. M. Wallace, 1981: Planetary-scale atmospheric phenomena associated with the southern oscillation. *Mon. Wea. Rev.*, **109**, 813–829, [https://doi.org/10.1175/1520-0493\(1981\)109<0813:PSAPAW>2.0.CO;2](https://doi.org/10.1175/1520-0493(1981)109<0813:PSAPAW>2.0.CO;2).
- Hsu, H. H., and J. M. Wallace, 1985: Vertical structure of wintertime teleconnection patterns. *J. Atmos. Sci.*, **42**, 1693–1710, [https://doi.org/10.1175/1520-0469\(1985\)042<1693:VSOWTP>2.0.CO;2](https://doi.org/10.1175/1520-0469(1985)042<1693:VSOWTP>2.0.CO;2).
- Hu, P., W. Chen, S. Chen, R. Huang, and Y. Liu, 2020: Extremely early summer monsoon onset in the South China Sea in 2019 following an El Niño event. *Mon. Wea. Rev.*, **148**, 1877–1890, <https://doi.org/10.1175/MWR-D-19-0317.1>.
- Huang, W., R. Chen, Z. Yang, B. Wang, and W. Ma, 2017: Exploring the combined effects of the Arctic Oscillation and ENSO on the wintertime climate over East Asia using self-organizing maps. *J. Geophys. Res. Atmos.*, **122**, 9107–9129, <https://doi.org/10.1002/2017JD026812>.
- Jeong, J.-H., and C.-H. Ho, 2005: Changes in occurrence of cold surges over East Asia in association with Arctic Oscillation. *Geophys. Res. Lett.*, **32**, L14704, <https://doi.org/10.1029/2005GL023024>.
- Johnson, N. C., S. B. Feldstein, and B. Tremblay, 2008: The continuum of Northern Hemisphere teleconnection patterns and a description of the NAO shift with the use of self-organizing maps. *J. Climate*, **21**, 6354–6371, <https://doi.org/10.1175/2008JCLI2380.1>.
- Joshi, M. K., and K. J. Ha, 2019: Fidelity of CMIP5-simulated teleconnection between Atlantic multidecadal oscillation and Indian summer monsoon rainfall. *Climate Dyn.*, **52**, 4157–4176, <https://doi.org/10.1007/s00382-018-4376-z>.
- Kalnay, E., and Coauthors, 1996: The NCEP/NCAR 40-Year Reanalysis Project. *Bull. Amer. Meteor. Soc.*, **77**, 437–471, [https://doi.org/10.1175/1520-0477\(1996\)077<0437:TNYRP>2.0.CO;2](https://doi.org/10.1175/1520-0477(1996)077<0437:TNYRP>2.0.CO;2).
- Kim, H.-J., and J.-B. Ahn, 2012: Possible impact of the autumnal North Pacific SST and November AO on the East Asian winter temperature. *J. Geophys. Res.*, **117**, D12104, <https://doi.org/10.1029/2012JD017527>.
- Kodera, K., 1998: Consideration of the origin of the different midlatitude atmospheric responses among El Niño events. *J. Meteor. Soc. Japan*, **76**, 347–361, [https://doi.org/10.2151/jmsj1965.76.3\\_347](https://doi.org/10.2151/jmsj1965.76.3_347).
- Koide, H., and K. Kodera, 1999: A SVD analysis between the winter NH 500-hPa height and surface temperature fields. *J. Meteor. Soc. Japan*, **77**, 47–61, [https://doi.org/10.2151/jmsj1965.77.1\\_47](https://doi.org/10.2151/jmsj1965.77.1_47).
- Kucharski, F., and M. K. Joshi, 2017: Influence of tropical South Atlantic sea-surface temperatures on the Indian summer monsoon in CMIP5 models. *Quart. J. Roy. Meteor. Soc.*, **143**, 1351–1363, <https://doi.org/10.1002/qj.3009>.
- Lau, N. C., 1988: Variability of the observed midlatitude storm tracks in relation to low-frequency changes in the circulation pattern. *J. Atmos. Sci.*, **45**, 2718–2743, [https://doi.org/10.1175/1520-0469\(1988\)045<2718:VOTOMS>2.0.CO;2](https://doi.org/10.1175/1520-0469(1988)045<2718:VOTOMS>2.0.CO;2).
- , and M. J. Nath, 1991: Variability of the baroclinic and barotropic transient eddy forcing associated with monthly changes in the midlatitude storm tracks. *J. Atmos. Sci.*, **48**, 2589–2613, [https://doi.org/10.1175/1520-0469\(1991\)048<2589:VOTBAB>2.0.CO;2](https://doi.org/10.1175/1520-0469(1991)048<2589:VOTBAB>2.0.CO;2).
- Lee, J., K. R. Sperber, P. J. Gleckler, C. J. W. Bonfils, and K. E. Taylor, 2019: Quantifying the agreement between observed and simulated extratropical modes of interannual variability.

- Climate Dyn.*, **52**, 4057–4089, <https://doi.org/10.1007/s00382-018-4355-4>.
- Lee, Y.-Y., J.-S. Kug, G.-H. Lim, and M. Watanabe, 2012: Eastward shift of the Pacific/North American pattern on an interdecadal time scale and an associated synoptic eddy feedback. *Int. J. Climatol.*, **32**, 1128–1134, <https://doi.org/10.1002/joc.2329>.
- Li, C., and J. J. Wettstein, 2012: Thermally driven and eddy-driven jet variability in reanalysis. *J. Climate*, **25**, 1587–1596, <https://doi.org/10.1175/JCLI-D-11-00145.1>.
- Li, X., Z.-Z. Hu, P. Liang, and J. Zhu, 2019: Contrastive influence of ENSO and PNA on variability and predictability of North American winter precipitation. *J. Climate*, **32**, 6271–6284, <https://doi.org/10.1175/JCLI-D-19-0033.1>.
- Lim, Y.-K., and H.-D. Kim, 2013: Impact of the dominant large-scale teleconnections on winter temperature variability over East Asia. *J. Geophys. Res. Atmos.*, **118**, 7835–7848, <https://doi.org/10.1002/jgrd.50462>.
- , and —, 2016: Comparison of the impact of the Arctic Oscillation and Eurasian teleconnection on interannual variation in East Asian winter temperatures and monsoon. *Theor. Appl. Climatol.*, **124**, 267–279, <https://doi.org/10.1007/s00704-015-1418-x>.
- Limpasuvan, V., D. L. Hartmann, D. W. J. Thompson, K. Jeev, and Y. L. Yung, 2005: Stratosphere–troposphere evolution during polar vortex intensification. *J. Geophys. Res.*, **110**, D24101, <https://doi.org/10.1029/2005JD006302>.
- Linkin, M. E., and S. Nigam, 2008: The North Pacific Oscillation–west Pacific teleconnection pattern: Mature-phase structure and winter impacts. *J. Climate*, **21**, 1979–1997, <https://doi.org/10.1175/2007JCLI2048.1>.
- Long, M., L. Zhang, S. Hu, and S. Qian, 2021: Multi-aspect assessment of CMIP6 models for Arctic sea ice simulation. *J. Climate*, **34**, 1515–1529, <https://doi.org/10.1175/JCLI-D-20-0522.1>.
- Lorenz, D. J., and D. L. Hartmann, 2003: Eddy–zonal flow feedback in the Northern Hemisphere winter. *J. Climate*, **16**, 1212–1227, [https://doi.org/10.1175/1520-0442\(2003\)16<1212:EFFITN>2.0.CO;2](https://doi.org/10.1175/1520-0442(2003)16<1212:EFFITN>2.0.CO;2).
- Moore, G. W. K., I. A. Renfrew, and R. S. Pickart, 2013: Multidecadal mobility of the North Atlantic Oscillation. *J. Climate*, **26**, 2453–2466, <https://doi.org/10.1175/JCLI-D-12-00023.1>.
- Nakamura, H., M. Tanaka, and J. M. Wallace, 1987: Horizontal structure and energetics of Northern Hemisphere wintertime teleconnection patterns. *J. Atmos. Sci.*, **44**, 3377–3391, [https://doi.org/10.1175/1520-0469\(1987\)044<3377:HTSAEON>2.0.CO;2](https://doi.org/10.1175/1520-0469(1987)044<3377:HTSAEON>2.0.CO;2).
- Nakamura, T., M. Hara, M. Oshika, and Y. Tachibana, 2015: Impact of the winter North Atlantic Oscillation (NAO) on the western Pacific (WP) pattern in the following winter through Arctic sea ice and ENSO. Part II: Multi-model evaluation of the NAO–ENSO linkage. *Climate Dyn.*, **45**, 3547–3562, <https://doi.org/10.1007/s00382-015-2556-7>.
- Nigam, S., 2003: Teleconnections. *Encyclopedia of Atmospheric Sciences*, J. R. Holton, J. A. Pyle, and J. A. Curry, Eds., Vol. 6, Academic Press, 2243–2269.
- , and S. Baxter, 2015: Teleconnections. *Encyclopedia of Atmospheric Sciences*, G. North, Ed., Elsevier Science, 90–109, <https://doi.org/10.1016/B978-0-12-382225-3.00400-X>.
- Ning, L., and R. S. Bradley, 2015: Winter climate extremes over the northeastern United States and southeastern Canada and teleconnections with large-scale modes of climate variability. *J. Climate*, **28**, 2475–2493, <https://doi.org/10.1175/JCLI-D-13-00750.1>.
- Nishii, K., H. Nakamura, and Y. J. Orsolini, 2010: Cooling of the wintertime Arctic stratosphere induced by the western Pacific teleconnection pattern. *Geophys. Res. Lett.*, **37**, L13805, <https://doi.org/10.1029/2010GL043551>.
- , —, and —, 2011: Geographical dependence observed in blocking high influence on the stratospheric variability through enhancement and suppression of upward planetary-wave propagation. *J. Climate*, **24**, 6408–6423, <https://doi.org/10.1175/JCLI-D-10-05021.1>.
- Notz, D., and SIMIP Community, 2020: Arctic sea ice in CMIP6. *Geophys. Res. Lett.*, **47**, e2019GL086749, <https://doi.org/10.1029/2019GL086749>.
- Orsolini, Y. J., A. Y. Karpechko, and G. Nikulin, 2009: Variability of the Northern Hemisphere polar stratospheric cloud potential: The role of North Pacific disturbances. *Quart. J. Roy. Meteor. Soc.*, **135**, 1020–1029, <https://doi.org/10.1002/qj.409>.
- Panagiotopoulos, F., M. Shahgedanova, and D. B. Stephenson, 2002: A review of Northern Hemisphere winter-time teleconnection patterns. *J. Phys. IV*, **12**, 1027–1047, <https://doi.org/10.1051/jp4:20020450>.
- Park, T.-W., C.-H. Ho, and S. Yang, 2011: Relationship between the Arctic Oscillation and cold surges over East Asia. *J. Climate*, **24**, 68–83, <https://doi.org/10.1175/2010JCLI3529.1>.
- Park, Y.-H., B.-M. Kim, G. Pak, M. Yamamoto, F. Vivier, and I. Durand, 2018: A key process of the nonstationary relationship between ENSO and the western Pacific teleconnection pattern. *Sci. Rep.*, **8**, 9512, <https://doi.org/10.1038/s41598-018-27906-z>.
- Piao, L., Z. Fu, and N. Yuan, 2016: “Intrinsic” correlations and their temporal evolutions between winter-time PNA/EPW and winter drought in the west United States. *Sci. Rep.*, **6**, 19958, <https://doi.org/10.1038/srep19958>.
- Rivière, G., 2010: Role of Rossby wave breaking in the west Pacific teleconnection. *Geophys. Res. Lett.*, **37**, L11802, <https://doi.org/10.1029/2010GL043309>.
- Rogers, J. C., 1981: The North Pacific Oscillation. *J. Climatol.*, **1**, 39–57, <https://doi.org/10.1002/joc.3370010106>.
- Sung, M.-K., H.-Y. Jang, B.-M. Kim, S.-W. Yeh, Y.-S. Choi, and C. Yoo, 2019: Tropical influence on the North Pacific Oscillation drives winter extremes in North America. *Nat. Climate Change*, **9**, 413–418, <https://doi.org/10.1038/s41558-019-0461-5>.
- , C. Yoo, S.-W. Yeh, Y. Kosaka, and S.-I. An, 2020: Characteristics of the North Pacific Oscillation in CMIP5 models in relation to atmospheric mean states. *J. Climate*, **33**, 3809–3825, <https://doi.org/10.1175/JCLI-D-19-0446.1>.
- Takaya, K., and H. Nakamura, 2005a: Mechanisms of intraseasonal amplification of the cold Siberian high. *J. Atmos. Sci.*, **62**, 4423–4440, <https://doi.org/10.1175/JAS3629.1>.
- , and —, 2005b: Geographical dependence of upper-level blocking formation associated with intraseasonal amplification of the Siberian high. *J. Atmos. Sci.*, **62**, 4441–4449, <https://doi.org/10.1175/JAS3628.1>.
- , and —, 2013: Interannual variability of the East Asian winter monsoon and related modulations of the planetary waves. *J. Climate*, **26**, 9445–9461, <https://doi.org/10.1175/JCLI-D-12-00842.1>.
- Tanaka, S., K. Nishii, and H. Nakamura, 2016: Vertical structure and energetics of the western Pacific teleconnection pattern. *J. Climate*, **29**, 6597–6616, <https://doi.org/10.1175/JCLI-D-15-0549.1>.
- Taylor, K. E., 2001: Summarizing multiple aspects of model performance in a single diagram. *J. Geophys. Res.*, **106**, 7183–7192, <https://doi.org/10.1029/2000JD900719>.

- , R. J. Stouffer, and G. A. Meehl, 2012: An overview of CMIP5 and the experiment design. *Bull. Amer. Meteor. Soc.*, **93**, 485–498, <https://doi.org/10.1175/BAMS-D-11-00094.1>.
- Thompson, D. W. J., and J. M. Wallace, 1998: The Arctic Oscillation signature in the wintertime geopotential height and temperature fields. *Geophys. Res. Lett.*, **25**, 1297–1300, <https://doi.org/10.1029/98GL00950>.
- , and —, 2000: Annular modes in the extratropical circulation. Part I: Month-to-month variability. *J. Climate*, **13**, 1000–1016, [https://doi.org/10.1175/1520-0442\(2000\)013<1000:AMITEC>2.0.CO;2](https://doi.org/10.1175/1520-0442(2000)013<1000:AMITEC>2.0.CO;2).
- , S. Lee, and M. P. Baldwin, 2003: Atmospheric processes governing the Northern Hemisphere annular mode North Atlantic Oscillation. *The North Atlantic Oscillation: Climatic Significance and Environmental Impact*, *Geophys. Monogr.* Vol. 134, Amer. Geophys. Union, 81–112, <https://doi.org/10.1029/134GM05>.
- Ulbrich, U., G. C. Leckebusch, and J. G. Pinto, 2009: Extra-tropical cyclones in the present and future climate: A review. *Theor. Appl. Climatol.*, **96**, 117–131, <https://doi.org/10.1007/s00704-008-0083-8>.
- Walker, G. T., and E. W. Bliss, 1932: World weather V. *Mem. Roy. Meteor. Soc.*, **4**, 53–84.
- Wallace, J. M., 2000: North Atlantic Oscillation/annular mode: Two paradigms—one phenomenon. *Quart. J. Roy. Meteor. Soc.*, **126**, 791–805, <https://doi.org/10.1002/qj.49712656402>.
- , and D. S. Gutzler, 1981: Teleconnections in the geopotential height field during the Northern Hemisphere winter. *Mon. Wea. Rev.*, **109**, 784–812, [https://doi.org/10.1175/1520-0493\(1981\)109<0784:TITGHF>2.0.CO;2](https://doi.org/10.1175/1520-0493(1981)109<0784:TITGHF>2.0.CO;2).
- Wang, G., D. Dommenges, and C. Frauen, 2015: An evaluation of the CMIP3 and CMIP5 simulations in their skill of simulating the spatial structure of SST variability. *Climate Dyn.*, **44**, 95–114, <https://doi.org/10.1007/s00382-014-2154-0>.
- Wang, X., M. Chen, C. Wang, S.-W. Yeh, and W. Tan, 2019: Evaluation of performance of CMIP5 models in simulating the North Pacific Oscillation and El Niño Modoki. *Climate Dyn.*, **52**, 1383–1394, <https://doi.org/10.1007/s00382-018-4196-1>.
- Wettstein, J. J., and J. M. Wallace, 2010: Observed patterns of month-to-month storm-track variability and their relationship to the background flow. *J. Atmos. Sci.*, **67**, 1420–1437, <https://doi.org/10.1175/2009JAS3194.1>.
- Willmott, C. J., and K. Matsuura, 2001: Terrestrial air temperature and precipitation: Monthly and annual time series (1950–1999). Center for Climatic Research, Department of Geography, University of Delaware, [http://climate.geog.udel.edu/~climate/html\\_pages/README\\_ghcn\\_ts2.html](http://climate.geog.udel.edu/~climate/html_pages/README_ghcn_ts2.html).
- Woo, S.-H., B.-M. Kim, J.-H. Jeong, S.-J. Kim, and G.-H. Lim, 2012: Decadal changes in surface air temperature variability and cold surge characteristics over northeast Asia and their relation with the Arctic Oscillation for the past three decades (1979–2011). *J. Geophys. Res.*, **117**, D18117, <https://doi.org/10.1029/2011JD016929>.
- Woollings, T., A. Charlton-Perez, S. Ineson, A. G. Marshall, and G. Masato, 2010: Associations between stratospheric variability and tropospheric blocking. *J. Geophys. Res.*, **115**, D06108, <https://doi.org/10.1029/2009JD012742>.
- Xu, T., Z. Shi, H. Wang, and Z. An, 2016: Nonstationary impact of the winter North Atlantic Oscillation and the response of mid-latitude Eurasian climate. *Theor. Appl. Climatol.*, **124** (1–2), 1–14, <https://doi.org/10.1007/s00704-015-1396-z>.
- Xu, Z., and K. Fan, 2020: Prolonged periodicity and eastward shift of the January North Pacific Oscillation since the mid-1990s and its linkage with sea ice anomalies in the Barents Sea. *J. Geophys. Res. Atmos.*, **125**, e2020JD032484, <https://doi.org/10.1029/2020JD032484>.
- Yang, Z., W. Huang, B. Wang, R. Chen, J. S. Wright, and W. Ma, 2018: Possible mechanisms for four regimes associated with cold events over East Asia. *Climate Dyn.*, **51**, 35–56, <https://doi.org/10.1007/s00382-017-3905-5>.
- Yeh, S.-W., X. Wang, C. Wang, and B. Dewitte, 2015: On the relationship between the North Pacific climate variability and the central Pacific El Niño. *J. Climate*, **28**, 663–677, <https://doi.org/10.1175/JCLI-D-14-00137.1>.
- , D.-W. Yi, M.-K. Sung, and Y. H. Kim, 2018: An eastward shift of the North Pacific Oscillation after the mid-1990s and its relationship with ENSO. *Geophys. Res. Lett.*, **45**, 6654–6660, <https://doi.org/10.1029/2018GL078671>.
- Yu, B., and X. Zhang, 2015: A physical analysis of the severe 2013/2014 cold winter in North America. *J. Geophys. Res. Atmos.*, **120**, 10 149–10 165, <https://doi.org/10.1002/2015JD023116>.
- , A. Shabbar, and F. W. Zwiers, 2007: The enhanced PNA-like climate response to Pacific interannual and decadal variability. *J. Climate*, **20**, 5285–5300, <https://doi.org/10.1175/2007JCLI1480.1>.
- Yu, J.-Y., and S. T. Kim, 2011: Relationships between extratropical sea level pressure variations and the central Pacific and eastern Pacific types of ENSO. *J. Climate*, **24**, 708–720, <https://doi.org/10.1175/2010JCLI3688.1>.
- Yuan, J., B. Tan, S. B. Feldstein, and S. Lee, 2015: Wintertime North Pacific teleconnection patterns: Seasonal and interannual variability. *J. Climate*, **28**, 8247–8263, <https://doi.org/10.1175/JCLI-D-14-00749.1>.
- Zappa, G., G. Masato, L. Shaffrey, T. Woollings, and K. Hodges, 2014: Linking Northern Hemisphere blocking and storm track biases in the CMIP5 climate models. *Geophys. Res. Lett.*, **41**, 135–139, <https://doi.org/10.1002/2013GL058480>.
- Zhao, W., S. F. Chen, W. Chen, S. Yao, D. Nath, and B. Yu, 2019: Interannual variations of the rainy season withdrawal of the monsoon transitional zone in China. *Climate Dyn.*, **53**, 2031–2046, <https://doi.org/10.1007/s00382-019-04762-9>.
- Zheng, X.-T., C. Hui, and S.-W. Yeh, 2018: Response of ENSO amplitude to global warming in CESM large ensemble: Uncertainty due to internal variability. *Climate Dyn.*, **50**, 4019–4035, <https://doi.org/10.1007/s00382-017-3859-7>.
- Zheng, Y. Q., S. F. Chen, W. Chen, and B. Yu, 2021: Diverse influences of spring Arctic Oscillation on the following winter El Niño–Southern Oscillation in CMIP5 models. *Climate Dyn.*, **56**, 275–297, <https://doi.org/10.1007/s00382-020-05483-0>.